



UNIVERSIDADE D
COIMBRA

Rui Miguel Grunert da Fonseca

LIGHT RESPONSIVE AND
MULTIFUNCTIONAL DENTAL IMPLANT
SYSTEMS

A MOLECULAR SIMULATION STUDY

Dissertation in the context of the Master in Chemical Engineering,
specialization in Chemical Processes, Environment and Energy, advised by
Professor Doctor Pedro Nuno das Neves Lopes Simões and Doctor Akhilesh
Rai, and presented to the Department of Chemical Engineering of the Faculty
of Sciences and Technology of the University of Coimbra.

September 2023



FACULDADE DE
CIÊNCIAS E TECNOLOGIA
UNIVERSIDADE DE
COIMBRA

DEPARTMENT OF CHEMICAL ENGINEERING

Rui Miguel Grunert da Fonseca

Light Responsive and Multifunctional Dental Implant Systems

A Molecular Simulation Study

Dissertation in the context of the Master in Chemical Engineering, specialization in Chemical Processes, Environment and Energy, advised by Professor Doctor Pedro Nuno das Neves Lopes Simões and Doctor Akhilesh Rai, and presented to the Department of Chemical Engineering of the Faculty of Sciences and Technology of the University of Coimbra.

September 2023



FACULDADE DE
CIÊNCIAS E TECNOLOGIA
UNIVERSIDADE DE
COIMBRA

DEPARTAMENTO DE ENGENHARIA QUÍMICA

Rui Miguel Grunert da Fonseca

Sistemas de Implantes Dentários Fotossensíveis e Multifuncionais

Estudo por Simulação Molecular

Dissertação no âmbito do Mestrado em Engenharia Química, especialização em Processos Químicos, Ambiente e Energia, orientada pelos Professor Doutor Pedro Nuno das Neves Lopes Simões e Doutor Akhilesh Rai, e apresentada ao Departamento de Engenharia Química da Faculdade de Ciências e Tecnologia da Universidade de Coimbra.

Setembro de 2023

Acknowledgements

This work was supported by a research grant in the scope of project "LightImplant" (PTDC/CTM-CTM/1719/2021), funded by the Portuguese Science Foundation ("Fundação para a Ciência e a Tecnologia, I.P./MCTES, FCT"), with national funds (PID-DAC). Access to computational resources of the Chemical Process Engineering and Forest Products Research Centre (CIEPQPF), supported by the Portuguese Science Foundation through FCT projects UIDB/EQU/00102/2020, UIDP/EQU/00102/2020, and 2022.15888.CPCA.A2, is gratefully acknowledged.

I would like to thank my advisors Prof. Pedro Nuno Simões and Dr. Akhilesh Rai for giving me the opportunity to carry out this project and for their invaluable support and encouragement.

I want to thank my colleagues for their companionship, and for creating a friendly atmosphere throughout this course.

I want to thank my family for all support and for encouraging me throughout this journey.

And lastly, I want to thank Inês for the companionship and joy we have shared these years.

Abstract

The rising demand of dental implants as a treatment for tooth loss has led to an increase in the incidence of peri-implant diseases, namely peri-implant mucositis and peri-implantitis. These diseases are usually a result of bacterial plaque buildup in the bases of the implants, which cause inflammation and, in some cases, bone deterioration. In an effort to reduce the occurrence of these diseases, a new implant material coated with black phosphorus and with the antimicrobial peptide LL37 is being studied. Potentially, it would allow the treatment of inflammation through photothermal therapy.

This study used Molecular Dynamics simulations considering a bacterial membrane model and the LL37 peptide conjugated with polyethylene glycol. These were performed considering different peptide concentrations at both 37 °C and 45 °C to emulate the increase of temperature during photothermal therapy. The effect of temperature and concentration on each membrane property was evaluated through the fitting of a multiple linear regression model and subsequent statistical analysis.

When in contact with the membrane, the LL37 peptide was shown to arrange itself in an α -helix structure, specifically in the sections of the residues 1-14 and 16-31. The hydrophobic residues were oriented towards the inside of the membrane, interacting with the phospholipid tails. On the other hand, the hydrophilic residues formed hydrogen bonds with the phosphate groups of the phospholipids. The presence of peptide also led to the displacement of potassium ions from the membrane surface.

An increase of temperature led to increases in the membrane fluidity and permeability, which allowed the peptide to insert itself in the membrane more easily. The membrane became thinner and the phospholipids were more easily displaced by the peptide. Overall, the increased temperature seemed to have a synergistic effect with the peptide, implying that the combination of photothermal therapy with antimicrobial peptide-coated materials may be a viable strategy for the prevention of peri-implant diseases.

Keywords

- Molecular Dynamics;
- Antimicrobial peptides;
- Peri-implant diseases.

Resumo

A crescente procura de implantes dentários para o tratamento de edentulismo tem levado ao aumento da incidência de doenças peri-implantares, nomeadamente a mucosite peri-implantar e a peri-implantite. Estas resultam de um acumular de placa bacteriana na base dos implantes, que por sua vez leva a inflamação dos tecidos moles, podendo levar, em alguns casos, à perda progressiva do osso de suporte. Numa tentativa de reduzir a ocorrência destas doenças, está a ser desenvolvido um novo material para uso em implantes dentários, revestido com fósforo preto e com o péptido antimicrobiano LL37. Este implante permitiria o tratamento da inflamação através da terapia fototérmica.

Este estudo utiliza uma metodologia de simulações de dinâmica molecular. O péptido LL37 conjugado com polietilenoglicol é simulado em conjugação com um modelo aproximado de uma membrana celular bacteriana, às temperaturas de 37°C e 45°C, simulando o efeito da terapia fototérmica. O efeito da temperatura e concentração de péptido na membrana foi estudado através de modelos de regressão linear ajustados a cada propriedade da membrana.

O péptido LL37, quando em contacto com a membrana, dispôs-se numa estrutura de alfa-hélice, principalmente nas secções dos aminoácidos 1-14 e 16-31. Os aminoácidos de cadeia lateral hidrofóbica inseriram-se dentro da membrana, e os aminoácidos hidrofílicos contribuíram para a fixação do péptido através da formação de ligações de hidrogénio com os grupos fosfato da membrana. O péptido também causou o deslocamento dos iões potássio para fora da superfície da membrana.

O aumento de temperatura levou ao aumento da permeabilidade da membrana, o que contribuiu para a mais fácil inserção do péptido. A membrana diminuiu de espessura e os fosfolípidos passaram a ter mais mobilidade. De forma geral, o aumento da temperatura pareceu potenciar a interação do péptido com a membrana celular. Isto significa que o uso de materiais revestidos com péptidos antimicrobianos juntamente com o uso da terapia fototérmica pode ser uma estratégia válida para a prevenção e tratamento de doenças peri-implantares.

Palavras-Chave

- Dinâmica molecular;
- Péptidos antimicrobianos;
- Doenças peri-implantares.

Contents

List of Figures	xvii
List of Tables	xxi
Preamble	xxiii
1 Introduction	1
1.1 Material design	1
1.2 Molecular Dynamics basics	2
1.3 Literature Review	6
1.3.1 Antimicrobial peptides	6
1.3.2 Membrane Model	8
1.3.3 Molecular Dynamics simulations	9
2 Methodology	11
2.1 Model definition	11
2.1.1 Physical model	11
2.1.2 Mathematical model	13
2.1.3 Simulation parameters	14
2.2 Experimental design	16
2.3 Data processing	17
3 Results and Discussion	21
3.1 General overview	21
3.2 Membrane properties	23
3.2.1 Thickness	23
3.2.2 Acyl chain order parameter	27
3.2.3 Lateral diffusion	29
3.2.4 Permeability	30
3.2.5 Area per lipid	33
3.2.6 Hydrogen bonds	36
3.3 Peptide-membrane interaction	38
3.3.1 Positioning and Forces	39
3.3.2 Hydrogen bonds	40

3.3.3	Ion displacement	46
3.4	Discussion	47
4	Conclusions and future perspectives	49
Appendix A Methodology		57
A.1	Parameter files (.mdp)	57
Appendix B Results and Discussion		65
B.1	Lipid tail order PCA analysis	65
B.2	Permeability – Poisson point process	66

Nomenclature

-CH₂-S-MAL-PEG CYS-MAL-PEG fragment side chain.

ALA alanine.

AMPs antimicrobial peptides.

APL area per lipid.

BP black phosphorus.

CL cardiolipin.

COM center of mass.

DPPG dipalmitoylphosphatidylglycerol.

FF force field.

LJ Lennard-Jones.

MD Molecular Dynamics.

MSD mean square displacement.

NIR near-infrared.

PBCs Periodic boundary conditions.

PC phosphatidylcholine.

PCA principal component analysis.

PE phosphatidylethanolamine.




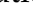
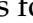
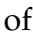
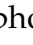
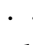
PG phosphatidylglycerol.

PID peri-implant diseases.

POPE 1-palmitoyl-2-oleoylphosphatidylethanolamine.

List of Figures

1	Peri-implant diseases (taken from Kormas et al. (2020)): (a) Peri-implant health; (b) Peri-implant mucositis; (c) peri-implantitis.	xxiii
1.1	Implant material representation (designed with Blender (Blender Online Community, 2018) and Pymol (Schrödinger, LLC, 2015)).	1
1.2	Simplified representation of a simulation box (highlighted box in the center).	2
1.3	Internal coordinates used in the calculation of bonded interactions.	3
1.4	General workflow of Molecular Dynamics (MD) simulations.	5
1.5	Representation of the AMP mechanism of action models (designed with Blender (Blender Online Community, 2018)).	7
1.6	Representation of the LL37 peptide chemical structure.	8
2.1	Creation of the cysteine+MAL+PEG residue topology file (.psf).	13
2.2	Representation of membrane thickness evaluation methodologies.	18
2.3	Illustration of the pre-selection procedure for one water molecule at a specific time point.	19
2.4	Trajectory analysis of 4 water molecules for the identification of events. Events are marked with an "×".	19
2.5	Example of a Voronoi diagram used for the calculation of the phospholipid areas (the highlighted area represents the simulation box and the darkened region represents the simulation box Periodic boundary conditions (PBCs)).	20
3.1	Snapshots of the systems' configuration after 1000 ns of simulation.	21
3.2	z-position of each LL37-PEG conjugates' center of mass (COM) vs time (LL37-PEG (—, —, —, —); membrane upper surface (—); time periods where membrane penetration is observed are highlighted with ■)	22
3.3	Membrane thickness vs. time of simulation without (left) or with (right) peptide penetration.	23
3.4	Membrane thickness linear regression.	24
3.5	Representation of the upper and lower membrane surfaces at specific time points.	25

3.6	Average membrane thickness (—) vs. 2 nd percentile (—) (simulations with membrane penetration: ).	26
3.7	S_{CH} parameters for each simulation and respective lipid-tail illustration (the lipid tails coloured in blue and red represent the maximum and minimum S_{CH} profiles).	27
3.8	S_{CH} -PC1 linear regression model.	28
3.9	Diffusion coefficient linear regression models for both dipalmitoylphosphatidylglycerol (DPPG) and 1-palmitoyl-2-oleoylphosphatidylethanolamine (POPE).	29
3.10	Counting of transmembrane crossings of water molecules throughout the simulation times.	31
3.11	Rate of transmembrane crossings of water molecules (λ) and its estimated standard deviation (represented with error bars) for each simulation.	31
3.12	Membrane permeability linear regression.	32
3.13	Representation of the phospholipid positioning and respective area for the "45-CM-rep1" simulation at two time points ($t = 50$ ns and $t = 800$ ns); The LL37-PEG position is represented through the COM of the amino acids (z-coordinate is represented with colour).	34
3.14	Average membrane area per lipid (APL) vs 98 th percentile (DPPG: average  , 98 th percentile  ; POPE: average  , 98 th percentile  ; Simulations with membrane penetration: ).	35
3.15	APL linear regression models for both DPPG and POPE.	36
3.16	Representation and labelling of the hydrogen donor and acceptor atoms of the phospholipid heads of DPPG and POPE.	37
3.17	Average number of hydrogen bonds between each donor and acceptor atom.	37
3.18	Linear regression model for the number of hydrogen bonds between membrane molecules.	38
3.19	Average z-coordinate of each amino acid over all peptides in the last 500 ns of all simulations (Hydrophobic amino acids:  ; Hydrophilic amino acids: ).	39
3.20	Average z-force exerted on each amino acid by the membrane (negative force values mean attractive forces).	40
3.21	Mean number of hydrogen bonds formed between each amino acid and the membrane, by residue order (left) and by descending order of the mean number of bonds (right).	42

3.22	Representation of both donor and acceptor atoms for each residue of the peptide, and respective average number of hydrogen bonds formed with the membrane. The average number of bonds is calculated considering all the peptides from all the simulations.	43
3.23	Representation of the LL37-PEG and average number of intra-peptide hydrogen bonds for simulations with and without a membrane.	45
3.24	Density profiles for each system component.	46
3.25	Potassium ion concentration color map (peptide: ■).	46
B.1	PC1 coefficients for the S_{CH} PCA analysis.	65
B.2	Histograms of inter-event times distributions.	66
B.3	P-P plot for the fitting of inter-event times to an exponential distribution.	67

List of Tables

1.1	List of antimicrobial peptides (AMPs) based on structure (adapted from Kumar et al. (2018)).	6
1.2	<i>E coli</i> lipid tail composition (adapted from Tan et al. (2017)).	9
1.3	MD simulations for the study of peptide and cell membrane interactions.	10
2.1	Molecular characteristics of the main species being simulated.	12
2.2	Composition of the simulation box.	12
2.3	Simulation parameters used for the system's energy minimization, equilibration and production runs.	15
2.4	List of simulations.	16
3.1	Membrane penetration time periods.	22
3.2	Parameter estimation for the membrane thickness regression model.	24
3.3	Parameter estimation for the S_{CH-PC1} regression model.	28
3.4	Parameter estimation for the diffusion coefficient regression models.	30
3.5	Parameter estimation for the membrane permeability regression models.	33
3.6	Parameter estimation for the APL regression models.	36
3.7	Parameter estimation for the regression model of the number of hydrogen bonds between membrane molecules.	38

Preamble

Dental implants, whose demand has been steadily increasing due to higher life expectancy, have been a widely popular treatment for tooth loss. Because bone requires stimulation to maintain form, the absence of a tooth leads to bone loss, which in turn can compromise the stability of adjacent teeth. Unlike other tooth loss treatments such as dentures, dental implants prevent bone loss by maintaining its supporting function (Resnik, 2019).

As in natural teeth, bacterial buildup in the bases of the implants can cause gum tissue inflammation, leading to the development of peri-implant diseases (PID) such as peri-implant mucositis and peri-implantitis. The latter implies bone deterioration, as shown in Figure 1, compromising the success rate of dental implants. Risk factors such as smoking and diabetes can contribute to the prevalence of PIDs (Parihar et al., 2020). Lee et al. (2017) reported that peri-implant mucositis and peri-implantitis have a patient prevalence of 46.8% and 19.8%, respectively.

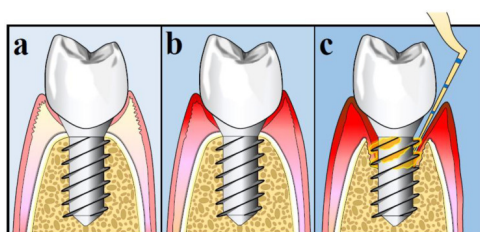


Figure 1: Peri-implant diseases (taken from Kormas et al. (2020)): (a) Peri-implant health; (b) Peri-implant mucositis; (c) peri-implantitis.

Dental implants can be made from pure titanium, titanium alloys (e.g., Ti-6Al-4V alloy) or zirconia, due to their ability to adhere to the bone surface – osseointegration. In recent years, new materials and technologies have been developed to prevent the formations of biofilms on implants, such as the use of barrier membranes (Sam, 2014).

This study addresses a light-responsive and multifunctional dental implant coated with black phosphorus (BP) and the AMP LL37 to control inflammation. The implant's BP coating allows the treatment of inflammation through the use of photothermal therapy, achieved by exposing the implant to near-infrared (NIR) light. This work tackles the effect of temperature on the interaction of the LL37 peptide with a bacterial membrane using MD simulations.

This document is organized as follows. Chapter 1 gives an introduction on MD simulations and presents literature regarding antimicrobial peptides (AMPs). In Chapter

2, the research methodology is presented. In Chapter 3, provides an analysis and discussion of the simulation data. The conclusions are presented in Chapter 4.

1. Introduction

1.1 Material design

This research aims to help the development of a light-responsive and multifunctional dental implant coated with black phosphorus (BP) and LL37 peptide to control inflammation using exposure to near-infrared (NIR) light. Exposure of the implant's BP coating to NIR light causes the production of thermal energy (photothermal effect), similarly to in Xie et al. (2020). The main goal of this research is to study the effect of temperature on the interaction of LL37 peptide with a bacterial membrane using Molecular Dynamics (MD) simulations.

As illustrated in Figure 1.1, the implant is made of the titanium alloy Ti-6Al-4V, and its surface is coated with a layer of BP. Cys-modified LL37 peptide conjugated with MAL-PEG-NH₂ is bonded to the BP surface via electrostatic adsorption, as described in Tao et al. (2016).

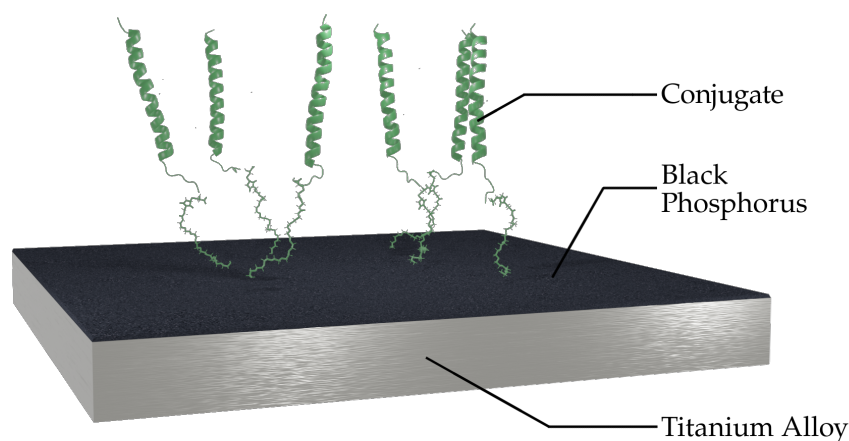


Figure 1.1: Implant material representation (designed with Blender (Blender Online Community, 2018) and Pymol (Schrodinger, LLC, 2015)).

1.2 Molecular Dynamics basics

MD simulations have been widely used to provide insight into the behavior of molecular systems in a variety of fields, such as chemical physics, materials science, biochemistry and chemical engineering. This type of simulation allows the detailed study of atomic-level phenomena which would otherwise not be achievable.

The recent development and improvement of mathematical models (force fields) has allowed the modelling of biological systems such as proteins, lipids and nucleic acids with increasing accuracy. This enables the study of mechanisms and interactions of drugs in biological systems.

Mathematical background

The physical model used in MD simulations consists of a number of point particles placed in a simulation box, as illustrated in Figure 1.2. These particles normally represent atoms, and their positions and momenta are described by classical mechanics.

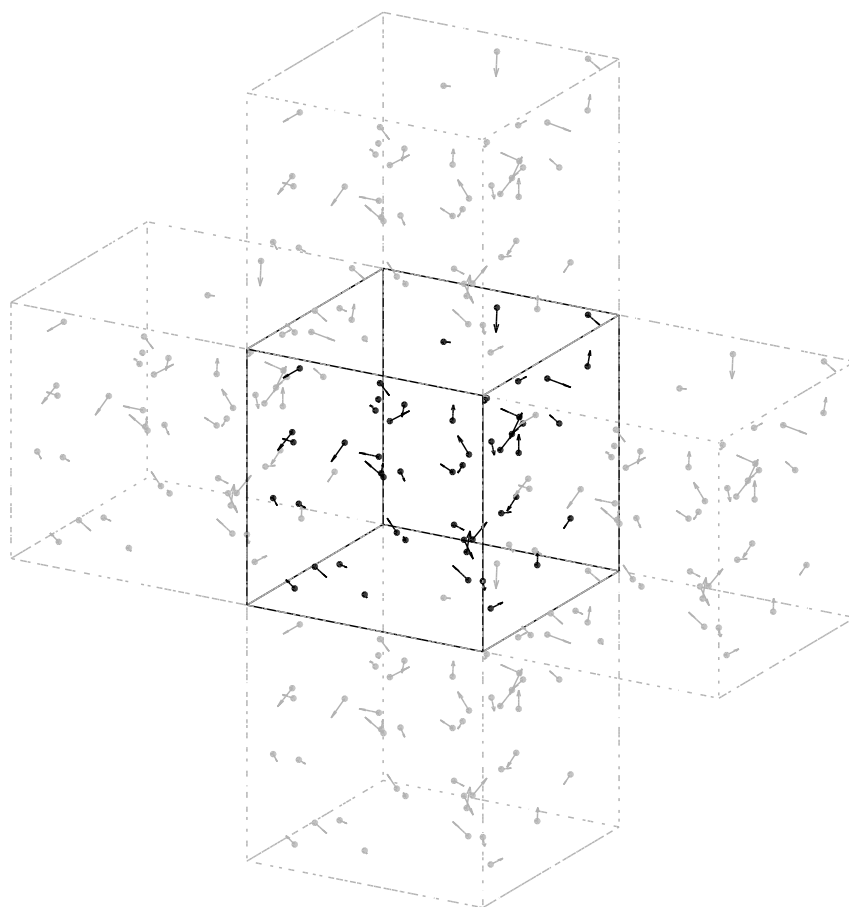


Figure 1.2: Simplified representation of a simulation box (highlighted box in the center).

The kinetic energy, E_k , of a system with N particles is calculated as the sum over all particles:

$$E_{k,\text{system}} = \sum_{i=1}^N E_{k,i} = \sum_{i=1}^N \frac{p_i^2}{2m_i} = \sum_{i=1}^N \frac{1}{2} m_i v_i^2 \quad (1.1)$$

where p_i , m_i and v_i are the momentum, mass and velocity of particle i .

The potential energy of the system, U , is given by the so-called force field (FF), which are sets of empirical functions that describe the different types of interactions between atoms. These functions are extensively parameterized based on experimental data and/or *ab initio* calculations. FFs account for two types of interactions: bonding interactions, which correspond to bonded atoms in a molecule, and non-bonding interactions, which include Van der Waals and electrostatic interactions.

Figure 1.3 illustrates the set of internal coordinates used in the calculation of bonded interactions.

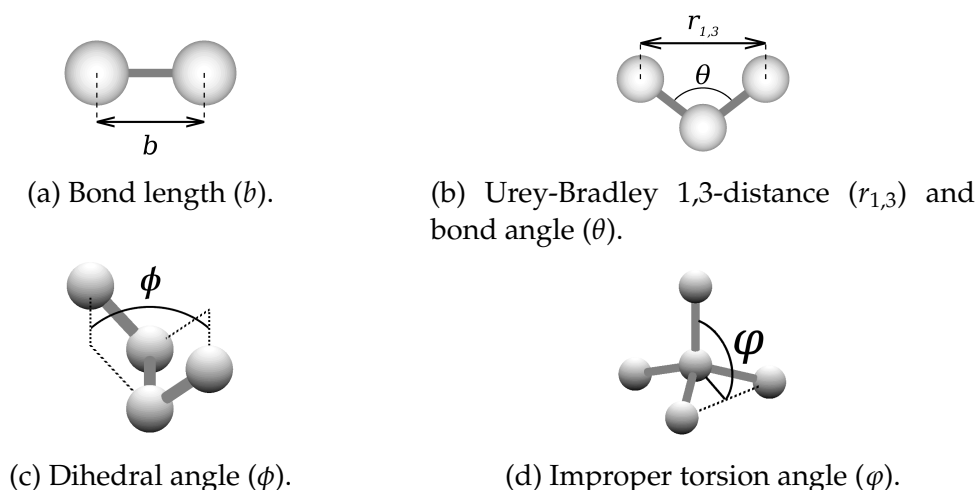


Figure 1.3: Internal coordinates used in the calculation of bonded interactions.

The potential energy associated to bond lengths can be modeled in a number of ways. The use of a harmonic oscillator with an equilibrium bond length of b_0 and constant K_b is common. The angular potential can also be modeled as a harmonic oscillator, in which θ_0 is the equilibrium bond angle and K_θ the stiffness constant. An additional harmonic potential regarding the distance between the non-central atoms of an angle (Urey-Bradley 1,3-distance, $r_{1,3}$) is used for some bond angles in the CHARMM36m FF. For molecules with four consecutively bonded atoms, there is an energy barrier associated with the rotation around the dihedral angles. This energy is modelled by a periodic function with the parameters periodicity (n), intensity (K_ϕ) and reference angle (ϕ_0). In some cases, these functions are not enough to describe the whole structure of a molecule. In particular, when in presence of planar groups, a harmonic potential

regarding the improper torsion angle (φ) is used. The combination of all these energy terms is expressed by Equation 1.2.

$$E_{\text{bonded}} = \sum_{\text{bond}} K_b (b - b_0)^2 + \sum_{\text{angle}} \left[K_\theta (\theta - \theta_0)^2 + K_{\text{UB}} (r_{1,3} - r_{1,3,0})^2 \right] \\ + \sum_{\text{dihedral}} K_\Phi [1 + \cos(n\phi - \phi_0)] + \sum_{\text{improper}} K_\varphi (\varphi - \varphi_0)^2 \quad (1.2)$$

The non-bonding interactions account for the electrostatic and Van der Waals forces between atoms. Because their number increases as the square of the number of particles, the computation of these energies becomes one of the most computationally demanding tasks of an MD simulation. Therefore, a cut-off distance is defined in order to exclude from these calculations the pairs of atoms separated by longer distances. The standard value for the cut-off distance is 1.2 nm. The Van der Waals and the electrostatic forces are mostly modelled using the Lennard-Jones (LJ) potential and the Coulomb's law, respectively. These are presented in Equation 1.3, where $r_{i,j}$ is the distance between atoms i and j , q_i and q_j are the charges of the atoms, $\sigma_{i,j}$ is the distance between atoms for which the LJ potential is zero, $\epsilon_{i,j}$ is the depth of the LJ potential well, and ϵ_0 is the vacuum permittivity.

$$E_{\text{nonbonded}} = \sum_{i,j} 4\epsilon_{i,j} \left[\left(\frac{\sigma_{i,j}}{r_{i,j}} \right)^{12} - \left(\frac{\sigma_{i,j}}{r_{i,j}} \right)^6 \right] + \sum_{i,j} \frac{q_i q_j}{4\pi\epsilon_0 r_{i,j}} \quad (1.3)$$

Deriving the different potential energy terms with respect to the position coordinates allows the calculation of the forces acting on each atom. The trajectories of the particles are then obtained through numerical integration of the equations of motion. The integration step needs to be small enough to accurately describe the highest frequency movement of the system: the oscillation of hydrogen atoms. A standard time step for these simulations is 2 fs.

Periodic boundary conditions (PBCs), as represented in Figure 1.2, are normally used to minimize boundary effects and to simulate the bulk system. The underlying algorithm allows the free movement of particles through the boundaries of the simulation box. The exit of a particle through one face of the box is compensated by another entering through the same position on the opposite face, thus ensuring that the number of particles in the simulation box remains constant. The use of PBCs can introduce periodic artifacts when a molecule interacts with its image. The simulation box must be big enough to assure that each molecule is at least the cut-off distance away from its image.

The direct use of MD leads to an NVE ensemble, since the system will have pre-determined volume and number of particles. Energy also remains constant since all the forces that make up the system are conservative forces. Most systems that are desired to be emulated have determined temperature and pressure values (NPT ensemble). To achieve constant pressure and temperature systems, pressure and temperature coupling algorithms must be implemented.

Constant temperature can be achieved through the use of velocity rescaling algorithms such as the ones proposed by Andersen (2008) or by Bussi et al. (2007). Alternatively, the implementation of a thermal reservoir that interacts with each particle of the system can also be used, as in the Nosé-Hoover thermostat, firstly proposed by Nosé (1984) and later modified by Hoover (1985).

Pressure control can be achieved through the scaling of the box size and the particle's coordinates. Scaling can be done by subjecting the box vectors to an equation of motion as in the Parrinello-Rahman barostat (Parrinello and Rahman, 1981), or by modifying the box size after every integration step, simulating an exponential relaxation of pressure to a reference value. Both Andersen (2008) as well as Bernetti and Bussi (2020) proposed algorithms following this principle.

The general procedure for MD simulations, as described in Figure 1.4, starts with the creation of the system's topology file and initial coordinates file. The particles' coordinates are then optimized by minimizing the potential energy of the system. To this point, no velocities were assigned to particles. Therefore, for the first equilibration step, velocities are generated based on the Maxwell-Boltzmann distribution for a specific temperature. The equilibration protocol should then allow the system to converge to the desired production run conditions. For some systems, a singular NVT equilibration run can suffice. For other more complex systems, equilibration strategies can include progressively decreasing positional constraints, the use of smaller integration steps, and the use of different temperature and pressure coupling algorithms.

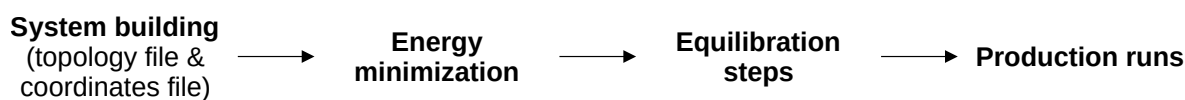


Figure 1.4: General workflow of MD simulations.

1.3 Literature Review

1.3.1 Antimicrobial peptides

Bacterial resistance to antibiotics has become a serious global health issue. Seen as a potential replacement to traditional antibiotics, antimicrobial peptides have become molecules of high interest. In general, antimicrobial peptides (AMPs) are considered less prone to antimicrobial resistance due to their multiple mechanisms of action (Ridyard and Overhage, 2021; Gan et al., 2021).

AMPs are found naturally in all forms of life. In bacteria, AMPs provide a way to kill competing species. In species with no adaptive immune system, such as plants and invertebrates, AMPs play a major role in the prevention of infections. In humans, only two types of AMPs are found: cathelicidins and defensins (Kumar et al., 2018).

AMPs are amphipathic and can present α -helix, β -sheet or extended structures. Table 1.1 lists some examples of AMPs for each type of structure.

Table 1.1: List of AMPs based on structure (adapted from Kumar et al. (2018)).

α -helix		β -sheet		Flexible	
Peptide	Source	Peptide	Source	Peptide	Source
Mellitin	Bees	Cathelicidins		Cathelicidins	
Citropin	Frogs	· Bactenecin	Bovine	· PR39	Pigs
Cathelicidins		Defensins		· Indolicidin	Bovine
· LL37	Humans	· α -defensins	Mammals	Histatins	Humans
· Cecropin	Insects	· β -defensins	Mammals		

Mechanism of action

Antimicrobial peptides have been shown to contribute to the killing of bacteria through different mechanisms of action, namely via immune modulation or direct killing of the bacteria (Kumar et al., 2018). The main mechanism of action is the direct killing of bacteria by targeting the cell membrane or other intracellular targets. Some AMPs, such as LL37, are also able to modulate immune responses by stimulating angiogenesis and attracting immune cells, thus controlling inflammation (Lai and Gallo, 2009; Nijnik and Hancock, 2009).

This study focuses solely on the mechanism of direct killing of bacteria through membrane targeting. Most AMPs are cationic with net charges of +2 up to +13 (Kumar et al., 2018), and are therefore attracted to the negative components of bacterial

membranes, namely the lipid heads of phosphatidylglycerol (PG) and cardiolipin (CL). Provided that enough concentration of peptide reaches the membrane, several models (illustrated in Figure 1.5) have been used to describe the peptide-membrane interaction (Oren and Shai, 1998; Kumar et al., 2018; Huan et al., 2020). Their main characteristics are described below.

Barrel-stave model: The AMPs perpendicularly penetrate the membrane forming a pore that causes cytoplasmic outflow. In this model, the amphipathic structure of the peptide (α -helix or β -sheet) plays an important role, since the hydrophobic side of the peptide interacts with the phospholipid tails of the membrane, and the hydrophilic side constitutes the inside walls of the channel.

Toroidal pore model: As in the previous model, the AMPs penetrate the membrane forming a pore. In this case, the peptides modify the hydrophobic/hydrophilic arrangement of the lipids, producing a local curvature of the membrane which leads to the formation of a channel.

Carpet model: Unlike the previous two models, the AMPs are adsorbed to the membrane forming a "carpet"-like structure which destabilizes the membrane. The cell membrane is destroyed with the formation of mycelles in a "detergent"-like manner. The required threshold concentration of peptide for this mechanism is high. LL37 is an example of an AMP which acts this way.

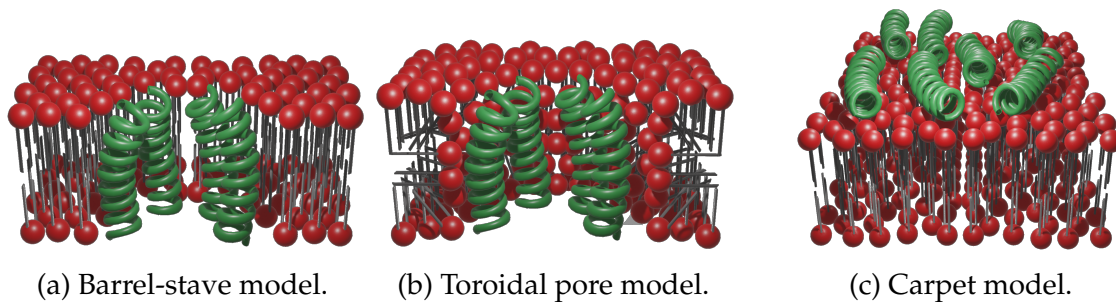


Figure 1.5: Representation of the AMP mechanism of action models (designed with Blender (Blender Online Community, 2018)).

LL37 Peptide

The LL37 Peptide (sketched in Figure 1.6) is the only cathelicidin found in humans, synthesized and released in epithelial cells, as well as in some immune cells. Considering the amino acid one-letter code, the peptide's amino acid sequence is:

LLGDFFRKSKEKIGKEFKRIVQRIKDFLRNLPRTES



Figure 1.6: Representation of the LL37 peptide chemical structure.

LL37 has been shown to facilitate bone regeneration in rats by promoting angiogenesis (Kittaka et al., 2013), and to play an important role in assuring oral cavity homeostasis by promoting mesenchymal stem cell differentiation, preventing bacteria-derived inflammation (Tokajuk et al., 2022).

1.3.2 Membrane Model

The membrane phospholipid composition plays a major role in the interaction of AMPs with it. For instance, AMP selectivity to bacteria is mainly attributed to the difference in membrane composition of eukaryotic and prokaryotic cells (Kumar et al., 2018). Therefore, the use of an appropriate membrane model is mandatory to achieve accurate results in MD simulations.

Bacterial membranes are predominately composed by phosphatidylethanolamine (PE) and have a net-negative charge from the phospholipid heads of PG and CL. This is an important factor in the initial electrostatic interaction with cationic AMPs. Eukaryotic membranes, as opposed to bacterial membranes, are mainly composed of the Zwitterionic phospholipid phosphatidylcholine (PC) and, for this reason, do not interact strongly with AMPs.

The phospholipid tail length and degree of saturation has an impact on the membrane thickness and fluidity, which in turn affects permeability. Phospholipid composition of a strain of gram-negative bacteria *E coli* was reported by Tan et al. (2017). The phospholipid head composition for this experiment's control strain was 8.8 % PG, 87.8 % PE and 3.3 % CL. The reported values for the phospholipid tail composition are

presented in Table 1.2.

Table 1.2: *E coli* lipid tail composition (adapted from Tan et al. (2017)).

Lipid tail	Composition (%)
C14:0	0.9 ± 0.2
C16:0	46.1 ± 0.7
C16:1	10.9 ± 0.3
C16-CH3	0.96 ± 0.02
C17cyc	15.0 ± 0.1
C18:0	2.3 ± 0.1
C18:1	21 ± 1
C18-OH	0.48 ± 0.01
C19cyc	2.5 ± 0.2

1.3.3 Molecular Dynamics simulations

Molecular Dynamics simulations have been widely used to study the interactions between peptides and cell membranes. Table 1.3 summarizes some of these simulations, presenting information on run simulation times, used membrane compositions and area.

Simulation physical times are highly dependent on the research subject. If only the initial peptide-membrane interaction is to be studied, then lower simulation times can be used. For some specific analyses, such as membrane permeability evaluation, longer simulation times are required for appropriate sampling and statistical analysis thereof, owing to the slower dynamics of the phenomenon. Bacterial membrane mimicking models always include about 20-25 % PG lipids and 70-80 % PE lipids. CL lipids are sometimes included at 5 % composition. Unsaturated lipid tails are usually considered by using the POPG and 1-palmitoyl-2-oleoylphosphatidylethanolamine (POPE) molecules. The considered membrane area is usually about 60-80 nm².

Table 1.3: MD simulations for the study of peptide and cell membrane interactions.

Reference	Run times	Membrane		Research subject
		Composition*	Area	
Zhao et al. (2018)	600 ns	pure POPG	256 lipids ($\approx 80 \text{ nm}^2$)**	LL37 selectivity evaluation for eukaryotic and procaryotic models
Sancho-Vaello et al. (2020)	200 ns	3:1 (POPE/DPPG)	64 nm^2	LL37 interaction with bacterial membrane considering a tetrameric channel structure
Chakraborty et al. (2020)	500 ns	<i>E. Coli</i> : 15:4:1; <i>S. Aureous</i> : 57:38:5 (PE/PG/CL)	<i>E. Coli</i> : $\approx 38 \text{ nm}^2$; <i>S. Aureous</i> : $\approx 80 \text{ nm}^2$	Interaction of two linear Battacin analogs with model gram-positive and gram-negative bacterial membranes
Vishweshwaraiah et al. (2021)	1.5 μs	3:1 (POPE/POPG)	121 nm^2	Peptide interaction with bacterial membrane for food preservation applications
Duay et al. (2019)	100 ns	4:1 (POPE/POPG)	120 lipids ($\approx 34 \text{ nm}^2$)**	Effect of zinc(II) on the structure and membrane interactions of the AMP Clavanin A
Ocampo-Ibáñez et al. (2020)	5 ns	<i>P aeruginosa</i> : 21:11:60; <i>K pneumoniae</i> : 82:6:5 (POPE/PMCL1/POPG)	186 lipids ($\approx 55 \text{ nm}^2$)**	Effect of membrane composition on peptide-membrane interactions considering the AMP CecD

*- bacterial membrane mimicking models

** - estimated based on the number of lipid molecules using CHARMM-GUI Membrane builder (Jo et al., 2009)

2. Methodology

2.1 Model definition

2.1.1 Physical model







The goal of this work is to gain knowledge on the atomistic scale features of the proposed dental implant material, namely the effect of the LL37 AMP conjugated with PEG (LL37-PEG) on the bacterial membrane. For this purpose, a simplified physical model of the actual system was conceived.

Unlike the real system, in which the peptide is linked to PEG through a linker (MAL) and both of these to the black phosphorous-titanium surface, only the LL37(-MAL)-PEG conjugate was considered. Furthermore, an oligomer instead of a polymer (PEG) was considered. On the other hand, the bacterial membrane was modeled using a symmetrical bilayer with the phospholipids POPE and dipalmitoylphosphatidylglycerol (DPPG). A molar ratio of 4:1 (POPE/DPPG) was used. Each molecule is described in more detail in Table 2.1.

The photothermal effect induced by the exposure of NIR light was modeled considering different temperatures, that is, performing simulations at 45 °C, in addition to the regular 37 °C (normal body temperature).

The simulation box was built using the membrane builder of the CHARMM-GUI toolbox (Jo et al., 2008). A lateral box width of 8 nm was selected, resulting in a membrane area of 64 nm². The membrane was placed in the center of the simulation box with a 4 nm-water layer on both the top and bottom of the system. This results in simulation box dimensions of approximately 8 nm × 8 nm × 11 nm. A concentration of 0.05 M of KCl was chosen, resembling human saliva (Nosek, 1998). Up to four LL37-PEG conjugates were placed 4-5 nm above the center of the simulation box, along the z-axis. The compositions of the different simulated systems are summarized in Table 2.2.

Table 2.1: Molecular characteristics of the main species being simulated.

LL37-PEG		
Description		
Peptide LL37 with added cysteine in the C-terminus Cysteine side-chain is modified with MAL-PEG		
Total charge	Number of Atoms	Molecular mass
+6	751	5166.2 Da
POPE		
Phospholipid class		Carbon tails
PE		16:0/ 18:1
Total charge	Number of Atoms	Molecular mass
0	125	718.01 Da
DPPG		
Phospholipid class		Carbon tails
PG		16:0/ 16:0
Total charge	Number of Atoms	Molecular mass
-1	123	721.98 Da
Atom color code: C - ; O - ; N - ; H - ; S - ; P - .		

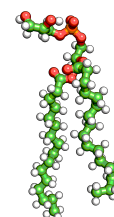
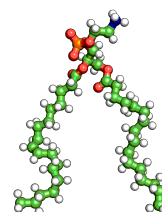
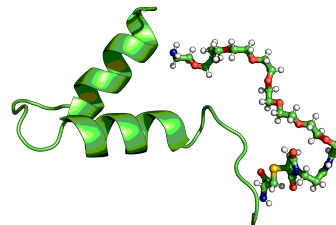


Table 2.2: Composition of the simulation box.

Molecule	N° of molecules	Total of atoms
LL37-PEG Conjugate	0 - 4	0 - 3004
POPE	176	22000
DPPG	44	5412
Water	14364 - 16029	43092 - 48087
Potassium ion	-	32 - 58
Chloride ion	-	12 - 14
Total	-	73584 - 75571

2.1.2 Mathematical model

The CHARMM36m (Huang et al., 2016) and lipid (Klauda et al., 2010; Venable et al., 2014) FFs were used for all molecular systems apart from the LL37-PEG conjugate, for which FF parameters were not readily available for the CYS-MAL-PEG fragment (CYL). Therefore, the following approach was used:

1. Topology and coordinate files for the CYS-MAL-PEG fragment side chain (-CH₂-S-MAL-PEG) were created by using the CHARMM-GUI "Ligand Reader & Modeler" tool (Kim et al., 2017). In both of these, an additional methyl (-CH₃) group in the α -carbon's position was considered replacing the amino acid backbone. The resulting structure was CH₃-CH₂-S-MAL-PEG.
2. A CHARMM topology file (.psf) for the CYS-MAL-PEG fragment was generated by adding the -CH₂-S-MAL-PEG moiety to the backbone of an amino acid, in this case alanine (ALA). As illustrated in Figure 2.1, this included:
 - Removing the additional methyl (-CH₃) group from the CH₃-CH₂-S-MAL-PEG structure, as well as the ALA side chain (also a -CH₃ group).
 - Correcting the difference in charges resulting from the removal of these groups (-CH₃), by adding the charge difference to the first carbon atom of the side chain (-CH₂-S-MAL-PEG).
 - Bonding the ALA α -carbon to the side chain.
3. ALA residue was added to the C-terminus of LL37 using the CHARMM-GUI "PDB Reader & Manipulator" tool.
4. The LL37-MAL-PEG conjugate coordinate file (.pdb) was generated by replacing the ALA side chain with -CH₂-S-MAL-PEG.
5. The conjugate topology file was then obtained through the CHARMM-GUI "PDB Reader & Manipulator" tool, based on the files created in step 2 and 4.

An additional 50-ns simulation of the conjugate in water was performed to obtain a starting configuration of the molecule for the main simulations.

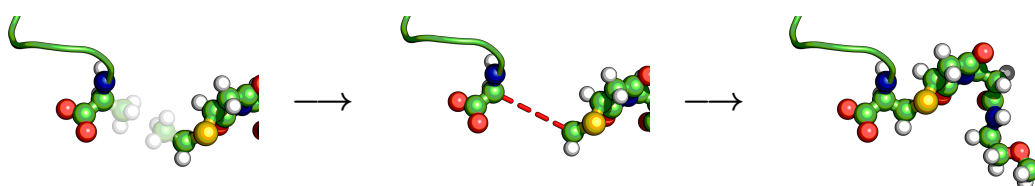


Figure 2.1: Creation of the cysteine+MAL+PEG residue topology file (.psf).

2.1.3 Simulation parameters

The production runs were performed with an NPT ensemble established by the use of the Nosé-Hoover thermostat (Nosé, 1984; Hoover, 1985) and the Parrinello-Rahman barostat (Parrinello and Rahman, 1981). The temperature is set to either 37°C or 45°C and the pressure to 1 bar. An integration time step of 2 fs was used to carry out the simulations.

The adopted equilibration protocol was based on the one proposed in the CHARMM-GUI toolbox (Jo et al., 2009). It consists of an initial system energy minimization, followed by six different equilibration steps, each with progressively weaker positional and dihedral restraints on the conjugate and phospholipid molecules. The integration time step was reduced to 1 fs in the first three equilibration steps, and in the first two an NVT ensemble was used instead of an NPT ensemble. The temperature and pressure coupling algorithms, "v-rescale" (Bussi et al., 2007) and "c-rescale" (Bernetti and Bussi, 2020) respectively, were used in all equilibration steps.

The simulation parameters are summarized in Table 2.3, and the complete ".mdp" files for each step are presented in section A.1 of the appendix.

Table 2.3: Simulation parameters used for the system's energy minimization, equilibration and production runs.

Energy minimization step						
Positional restraints (kJ mol ⁻¹ nm ⁻²)						
Backbone						4000
Backbone Sidechain						2000
Phosporus z-position						1000
Dihedrals restraints (kJ mol ⁻¹ rad ⁻²)						
Lipids*						1000
Max. force (kJ mol ⁻¹ nm ⁻¹)						
						1000
Equilibration steps						
	Step 1	Step 2	Step 3	Step 4	Step 5	Step 6
Positional restraints (kJ mol ⁻¹ nm ⁻²)						
Backbone	4000	2000	1000	500	200	50
Sidechains	2000	1000	500	200	50	0
Phosporus z-position	1000	400	400	200	40	0
Dihedrals restraints (kJ mol ⁻¹ rad ⁻²)						
Lipids*	1000	400	200	200	100	0
Ensemble						
Temperature coupling V-rescale					
Pressure coupling	×	× C-rescale			
Time step (fs)	1	1	1	2	2	2
Simulation time (ps)	125	250	250	500	500	500
Production run						
Ensemble						
Temperature coupling	Nosé-Hoover					
Pressure coupling	Parrinello-Rahman					
Time step (fs)	2					
Simulation time (ns)	1000					

*-includes:

- glycerol's central C-atom improper dihedral for both lipids
- glycerol 3-phosphate's central C-atom improper dihedral in DPPG's head
- the double bond dihedral from the POPE's unsaturated carbon tail

2.2 Experimental design

This study aims to evaluate the impact of temperature and concentration of AMP on the following features:

- Bacterial membrane properties, namely thickness, permeability, lipid tail order parameters and area per lipid.
- Peptide-specific responses, such as positioning and the number of intramolecular hydrogen bonds.
- Peptide-membrane interactions, in particular the number of hydrogen bonds and intermolecular forces between both types of molecules.

The simulations were planned according to a factorial design with two levels for temperature (37 °C and 45 °C) and four levels for AMP concentration (0, 1, 2 and 4 conjugates). A total of two 1- μ s runs were done for each instance, except for the 4-conjugate simulations in which only one run was done. Table 2.4 summarizes and labels the experiments carried out. For each temperature, an additional two 1- μ s simulations were carried out, considering only the peptide in solution without a membrane, to use as reference in the analysis of peptide properties.

Table 2.4: List of simulations.

Temperature	N° of AMPs	Labels	
		run 1	run 2
Peptide+membrane simulations			
37 °C	0	37C-SM-rep1	37C-SM-rep2
	1	37C-CM-rep1	37C-CM-rep2
	2	37C-2CM-rep1	37C-2CM-rep2
	4	37C-4CM-rep1	-
.....			
45 °C	0	45C-SM-rep1	45C-SM-rep2
	1	45C-CM-rep1	45C-CM-rep2
	2	45C-2CM-rep1	45C-2CM-rep2
	4	45C-4CM-rep1	-
Peptide-only simulations			
37 °C	1	37C-SP-rep1	37C-SP-rep2
45 °C	1	45C-SP-rep1	45C-SP-rep2

2.3 Data processing

In this section, the procedures used to treat the data from the simulations are described. These include thickness evaluation, permeability evaluation and area per lipid calculation.

Membrane thickness evaluation

The membrane thickness was evaluated based on the membrane and water density profiles obtained by the GROMACS analysis tools `gmx density` and `gmx densmap`. These profiles were used to define the upper and lower membrane surfaces. The difference of the two results in the membrane thickness.

For simulations with no conjugated peptides, the upper and lower surfaces could technically be defined by the points (z_{up} and z_{low}) in which the values of water and membrane density (ρ_{wat} and ρ_{mem}) are equal, that is, z_{up} and z_{low} are the solutions of

$$\rho_{\text{mem}}(z) = \rho_{\text{wat}}(z). \quad (2.1)$$

However, for simulations including the LL37-MAL-PEG conjugate, the displacement of water caused by the peptides would deviate the determined surface location away from the center of the membrane, as shown in Figure 2.2. This would result in an overestimation of the thickness. A modified procedure for the definition of the membrane surfaces was therefore adopted:

1. Calculation of the corresponding average membrane density in the locations of the membrane surfaces (ρ_{mean}) for each temperature, using the data from the non-peptide simulations, considering the previous criteria. This is

$$\rho_{\text{mean}} = \langle [\rho_{\text{mem}}(z_{\text{up}}), \rho_{\text{mem}}(z_{\text{low}})] \rangle. \quad (2.2)$$

2. Definition the membrane surfaces using these values as a reference, that is, z_{up} and z_{low} are the solutions of

$$\rho_{\text{mem}}(z) = \rho_{\text{mean}} \quad (2.3)$$

This way, the presence of peptides does not interfere with the calculation of the membrane thickness.

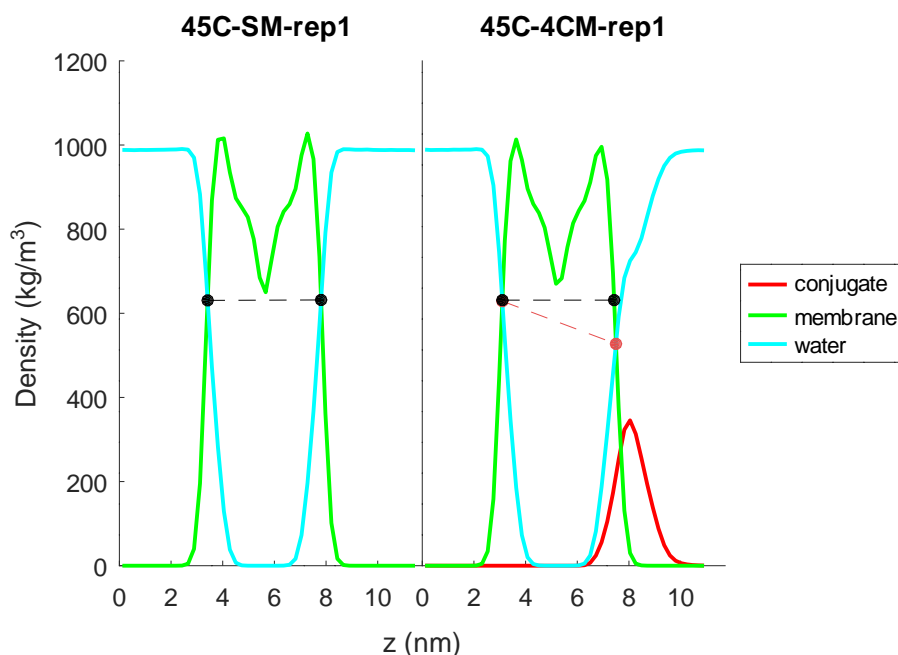


Figure 2.2: Representation of membrane thickness evaluation methodologies.

Membrane permeability

The membrane permeability to water was evaluated by determining the number of times a water's oxygen atom passed through the membrane. This occurrence will, from now on, be referred to as an event. Similarly to Venable et al. (2019), the procedure was performed as follows:

1. The water molecules whose trajectory included at least one point inside a 1.5 nm height box vertically centered in the membrane were pre-selected, as illustrated in Figure 2.3. This was done to reduce the number of analyzed trajectories and achieved using the gromacs analysis tool `gmx select` with the following selection command:

```
group "SOLV" and name OH2 and z > 5.0203 and z < 6.5203;
```

2. The trajectories of the pre-selected molecules were then obtained through the `gmx traj` analysis tool using the option `-nojump yes`.
3. An event was counted every time a water molecule fully traveled across a 2 nm height box, also vertically centered in the membrane, as in Figure 2.4. This time, a 2 nm box was used to avoid the counting of events in which water molecules penetrated the membrane and immediately returned to their original side of the box.

4. The initial and final xy position of the water molecule, as well as the time interval in which the event occurred were recorded.

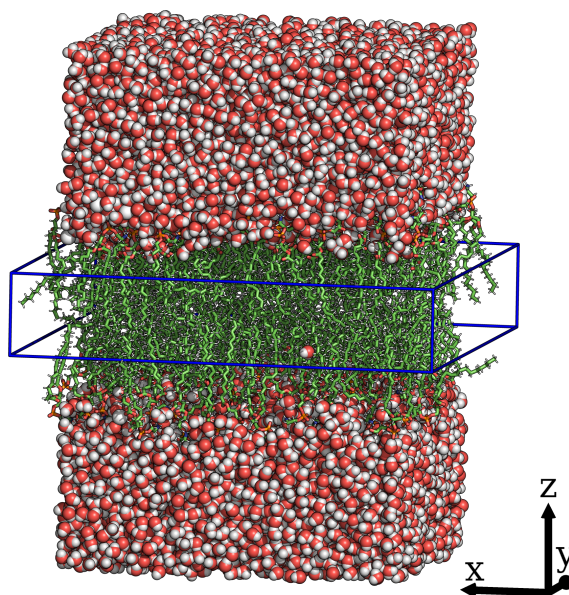


Figure 2.3: Illustration of the pre-selection procedure for one water molecule at a specific time point.

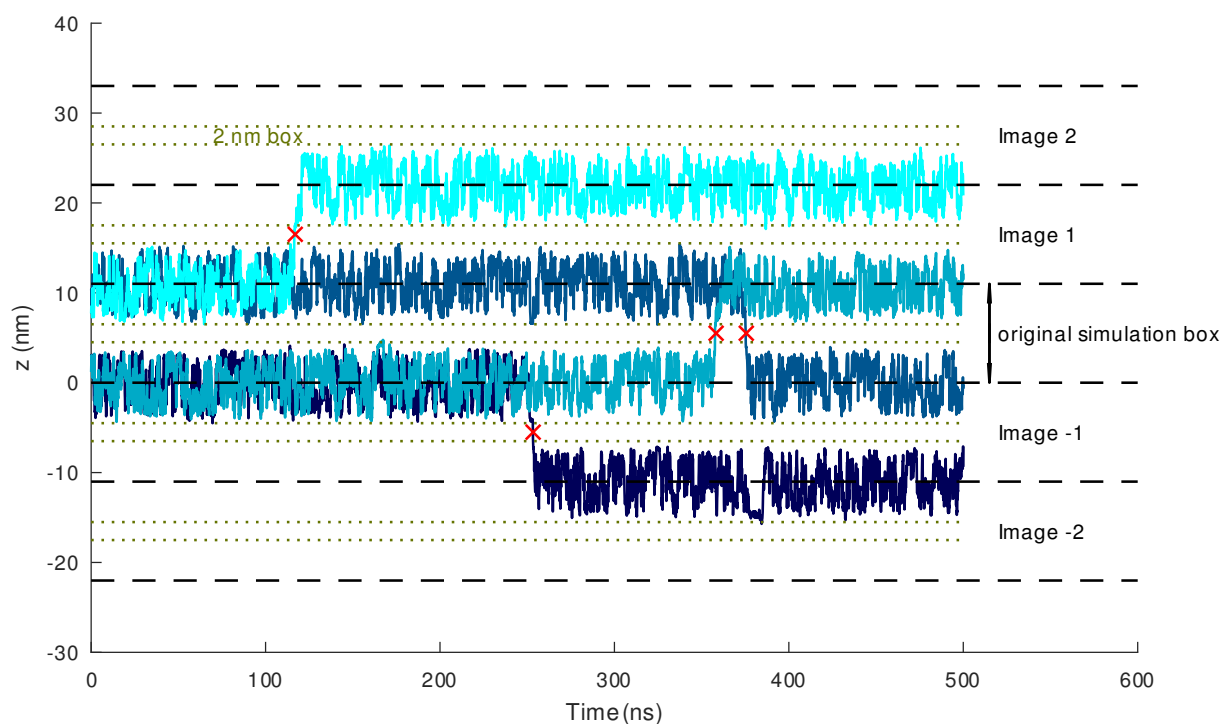


Figure 2.4: Trajectory analysis of 4 water molecules for the identification of events. Events are marked with an "X".

Area per lipid

The area occupied by each lipid in the xy -plane was defined considering the position of the center of mass of each phospholipid. Two Voronoi diagrams – one per leaflet of the bilayer – were drawn in every frame of each simulation based on the positions of each phospholipid. The resulting convex polygons' areas were calculated, considering PBCs and their values assigned to the corresponding lipid molecule in that specific frame. This is illustrated in Figure 2.5.

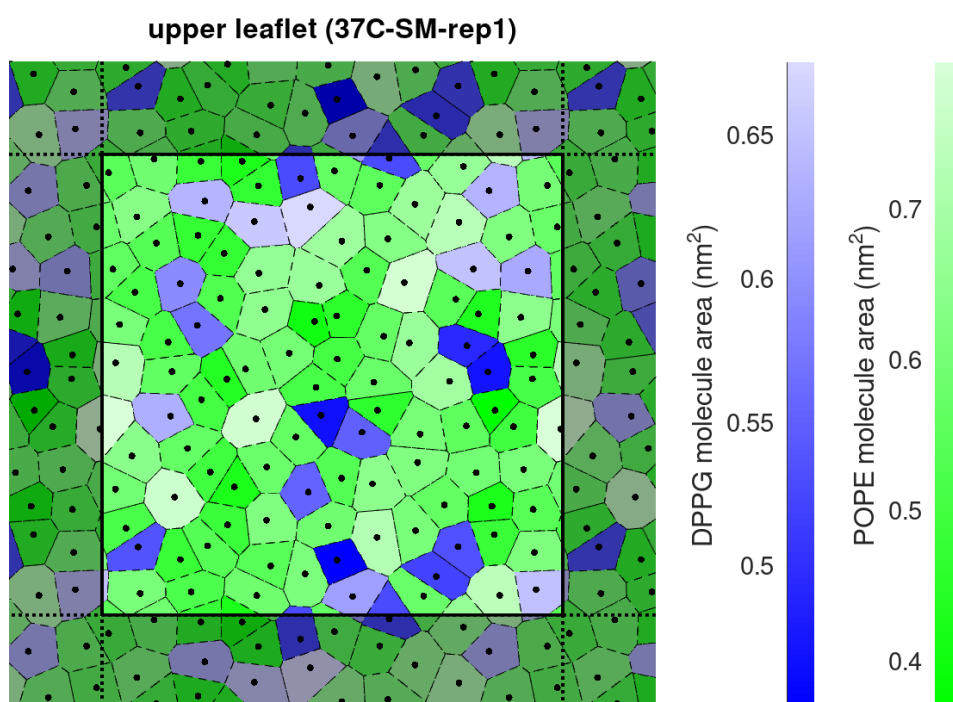


Figure 2.5: Example of a Voronoi diagram used for the calculation of the phospholipid areas (the highlighted area represents the simulation box and the darkened region represents the simulation box PBCs).

3. Results and Discussion

In this chapter, the resulting data from each simulation and their statistical analysis are presented. The MD trajectories were processed and analyzed with GROMACS tools, while the statistical analysis was carried out with GNU Octave (<https://octave.org/>).

3.1 General overview

In the total accumulated physical time of 14 μ s of simulations, no major pore formations were observed in the membrane (Figure 3.1), which is understandable given that the dynamics of this phenomenon should require the simulation of longer physical times. Even so, the results are still enough to reveal the interaction between the LL37-PEG conjugate and the membrane, particularly in terms of how the membrane's properties are affected.

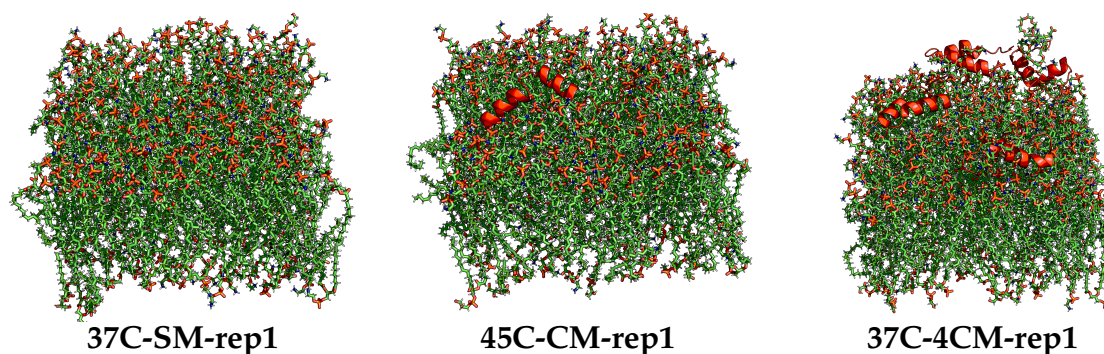


Figure 3.1: Snapshots of the systems' configuration after 1000 ns of simulation.

From the very beginning of the simulations (initial 50 ns), the LL37-PEG conjugate diffused and then adhered to the upper membrane surface. The geometrical arrangement of the participating peptides resembled that of the Carpet model, in that they would be oriented parallel to the membrane surface. Throughout the simulations, there were particular instances where a peptide would dig deeper into the membrane, remaining there either for certain time intervals or until the end of the simulations. Although this occurrence did not include all the conjugates, it was prevalent in the simulations at 45°C. This can be seen in Figure 3.2, which plots the z-position of cen-

ter of mass (COM) of each LL37-PEG conjugate throughout each simulation. Table 3.1 summarizes the time frames of each one of these periods.

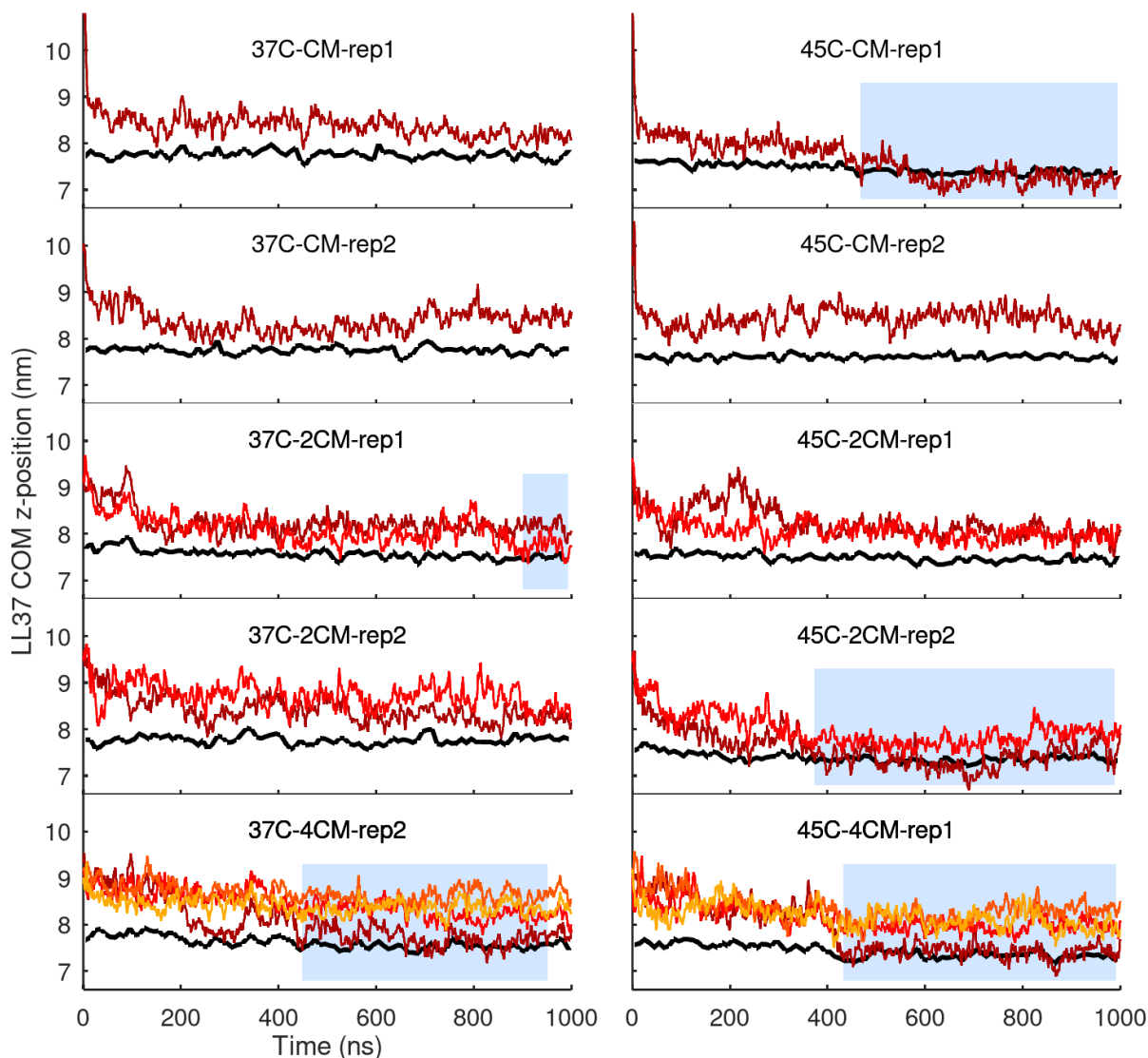


Figure 3.2: z -position of each LL37-PEG conjugates' COM vs time (LL37-PEG (—, —, —, —)); membrane upper surface (—); time periods where membrane penetration is observed are highlighted with)

Table 3.1: Membrane penetration time periods.

Simulation	Time interval (ns)
37C-2CM-rep1	900.7 - 993.7
37C-4CM-rep2	448.0 - 950.8
45C-CM-rep1	467.7 - 995.0
45C-2CM-rep2	373.2 - 988.9
45C-4CM-rep1	432.5 - 990.8

3.2 Membrane properties

To evaluate the influence of temperature (T) and concentration of peptide (C) on the membrane, a multiple linear regression model was fitted to each membrane property data. Each models' parameters (b_i) and respective variances were estimated, and a two-sided Student's t-test ($\alpha = 0.05$) was done to determine if the null hypothesis (Equation 3.1 – membrane property value is not affected by the independent variable) could be rejected.

$$H_0 : b_i = 0 \quad (3.1)$$

3.2.1 Thickness

The membrane thickness was evaluated over the simulation time and the data are illustrated in Figure 3.3. In the simulations where membrane penetration did not occur, membrane thickness remained relatively stable. "45C-2CM-rep1" did experience a slight drop in thickness (≈ 0.031 nm or 0.7 %), but not as pronounced as in the simulations with membrane penetration, in which thickness decreased approximately 0.129 nm (≈ 2.9 % of the initial thickness) in the first 500 ns of simulation.

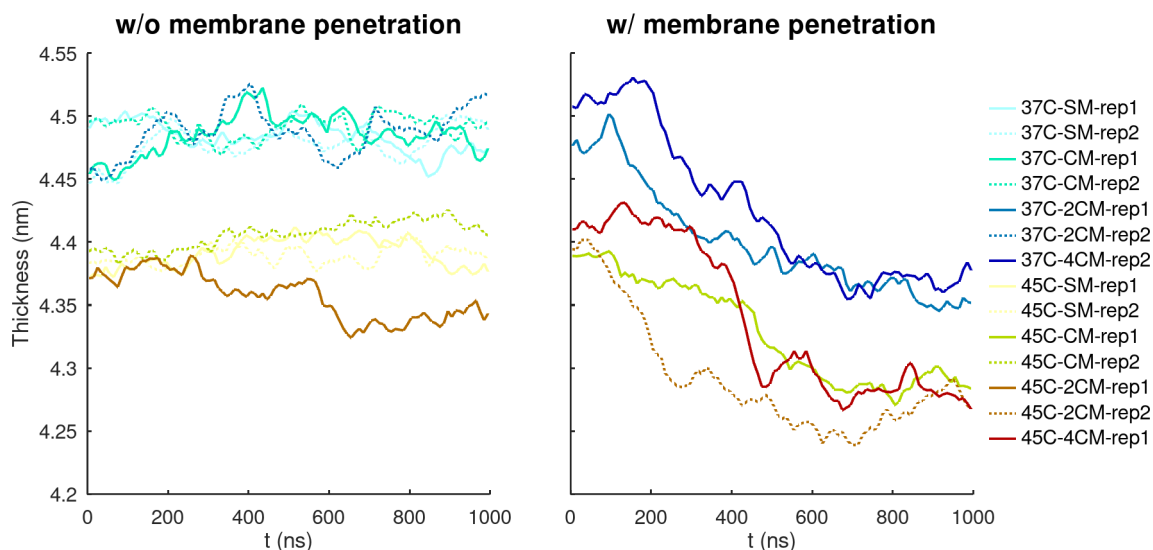


Figure 3.3: Membrane thickness vs. time of simulation without (left) or with (right) peptide penetration.

The average thickness of the last 300 ns of each simulation (700-1000 ns) was used for the linear regression model. The data are plotted in Figure 3.4 and the parameter estimation is summarized in Table 3.2. The increase in temperature resulted in an average decrease in thickness ($b_T \times \Delta T$) of 0.11 nm ($\approx 2.5\%$). The effect of peptide concentration is not as clear as that of temperature, since a decrease in thickness happened

mostly when membrane penetration was observed. With that being said, at larger timescales membrane penetration is expected to happen at some point, which would then result in a decrease in thickness. The temperature-concentration interaction factor ($b_{T \times C}$) was not statistically significant (p-value=0.99), and so it was not considered.

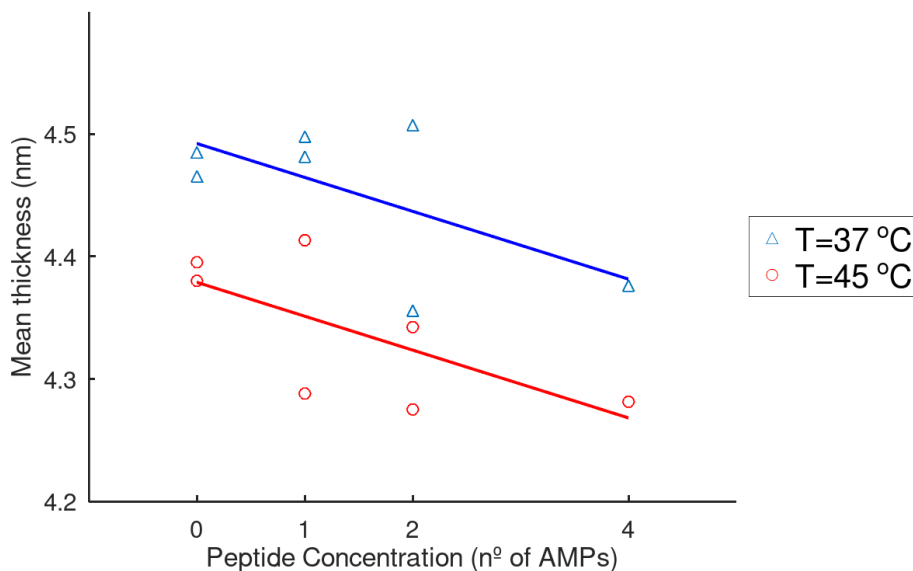


Figure 3.4: Membrane thickness linear regression.

Table 3.2: Parameter estimation for the membrane thickness regression model.

Model: $Y = a + b_T T + b_C C$			
Parameter	Estimate	Confidence Interval (95 %)	p-value ($\alpha = 0.05$)
a	5.02	[4.73, 5.30]	<0.001
b_T	-0.0142	[-0.0211, -0.0072]	<0.001
b_C	-0.0277	[-0.0492, -0.0061]	0.017

The membrane thickness was also evaluated locally considering a 16×16 grid in the xy -plane, as illustrated in Figure 3.5. The membrane surfaces are relatively smooth without the presence of peptide. When peptides are present, the membrane's upper surface caves in, decreasing the local membrane thickness.

The membrane thickness distribution was analyzed to evaluate the local decrease in thickness caused by the peptides. The 2nd percentile of thickness is plotted against the corresponding thickness average for each frame of simulation in Figure 3.6. The 2nd percentile was chosen instead of the minimum, as it is a more stable statistic. As expected, the simulations in which membrane penetration occurred had big drops in the 2nd percentile metric after some simulation time. The difference in thickness between the average and the 2nd percentile was as high as 1.12 nm ($\approx 27.4\%$ of the average). In

comparison, when there was no peptide, the metric remained stable and the difference between metrics was about 0.17 nm ($\approx 9.4\%$). This shows that the peptide effect on the membrane thickness is mainly local.

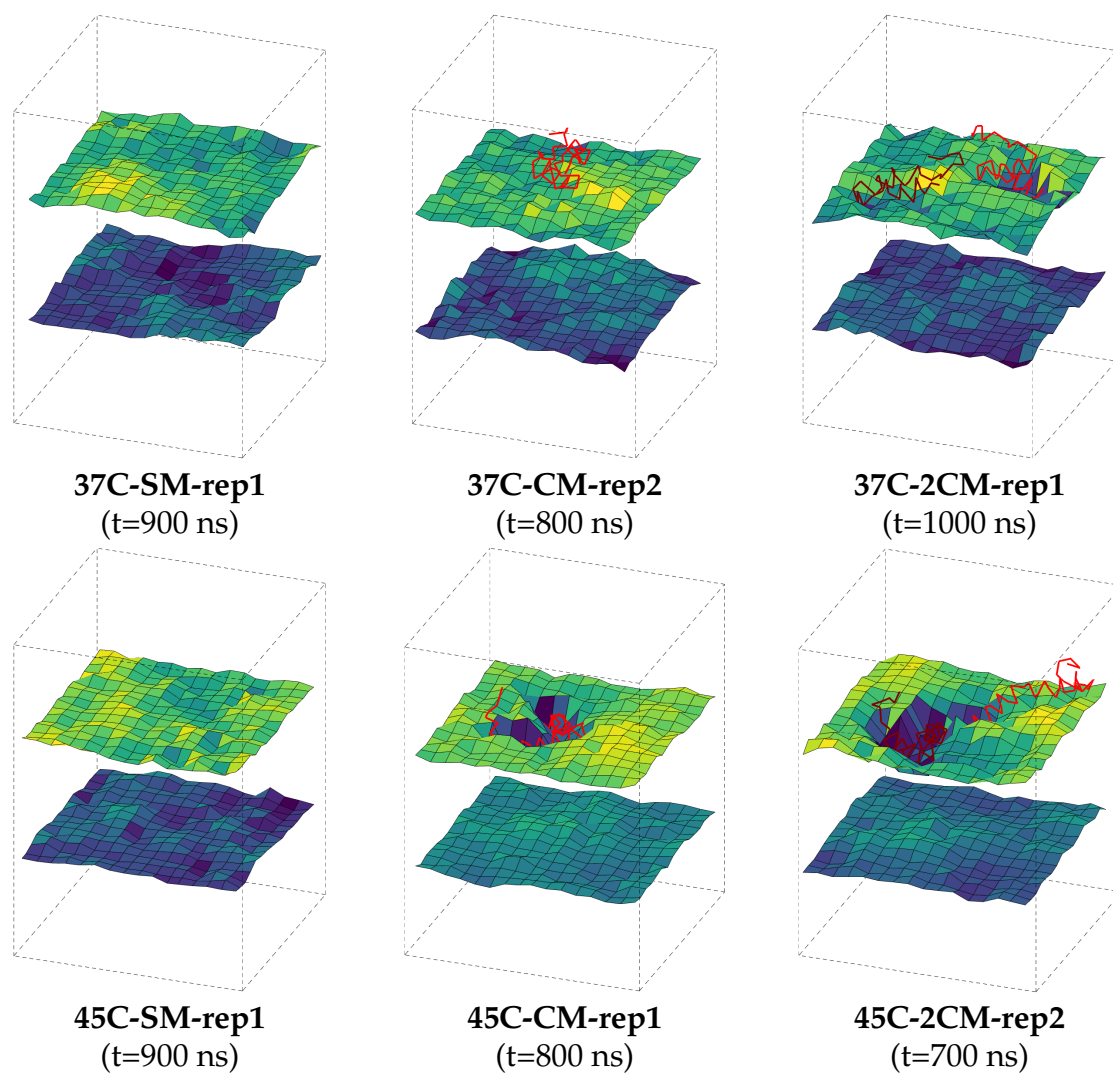


Figure 3.5: Representation of the upper and lower membrane surfaces at specific time points.

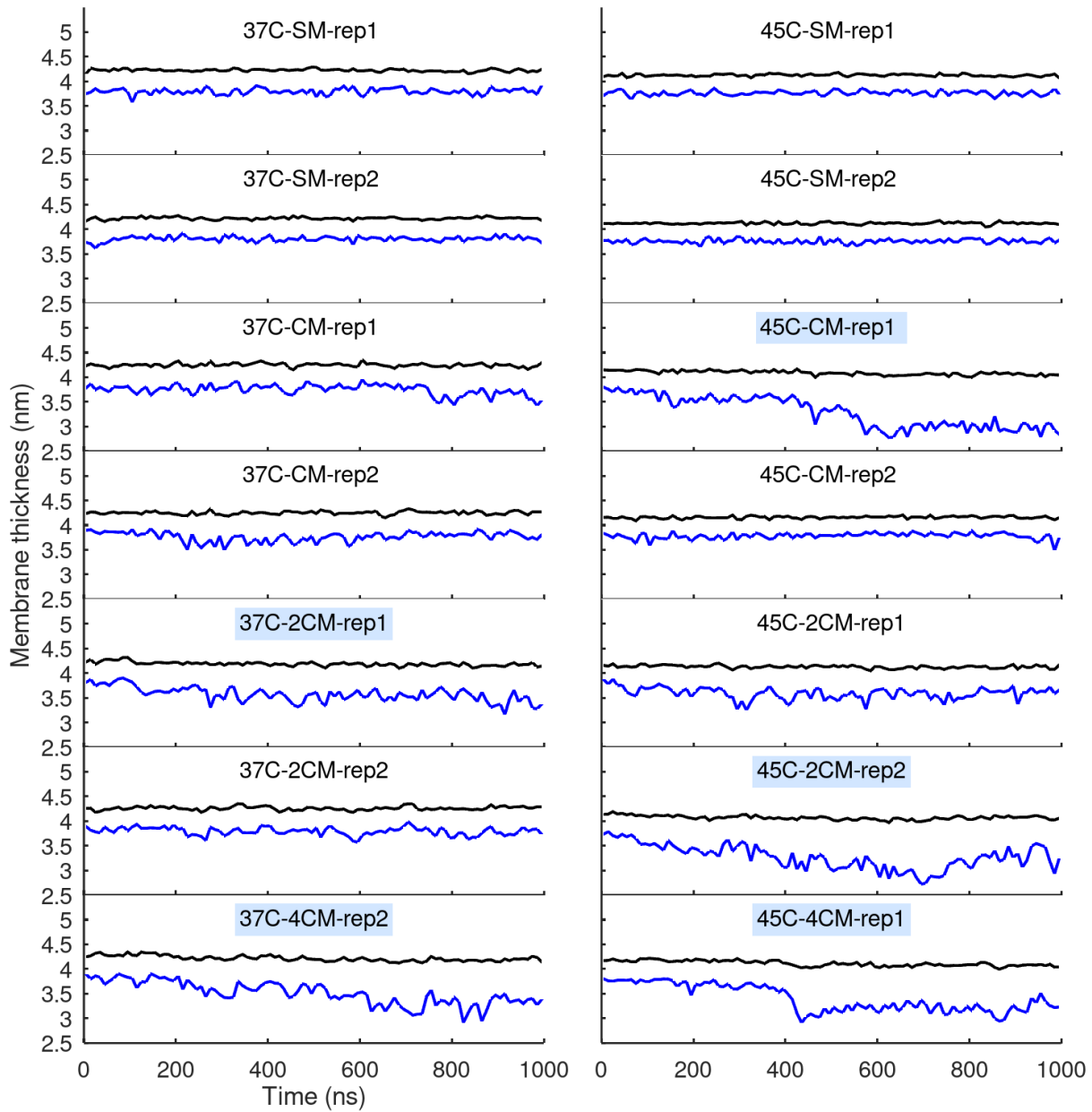


Figure 3.6: Average membrane thickness (—) vs. 2nd percentile (—) (simulations with membrane penetration: ■).

3.2.2 Acyl chain order parameter

As determined in Equation 3.2, the lipid acyl chain parameter (S_{CH}) is calculated based on the average orientation of the C–H bonds of the lipid tail, over all lipids and simulation time, in regards to membrane normal, i.e. the z-axis, according to Piggot et al. (2017):

$$S_{CH} = \langle 3 \cos^2 \theta - 1 \rangle / 2 \quad (3.2)$$

where θ is the angle between the C–H bond and the z-axis.

Lower S_{CH} values imply that the C–H bonds are mostly parallel to the membrane surface, resulting in a more vertically oriented lipid tail. Figure 3.7 displays the obtained S_{CH} simulation profiles for DPPG and for POPE's both saturated and unsaturated chains, as well as visual representations for the minimum and maximum S_{CH} profiles.

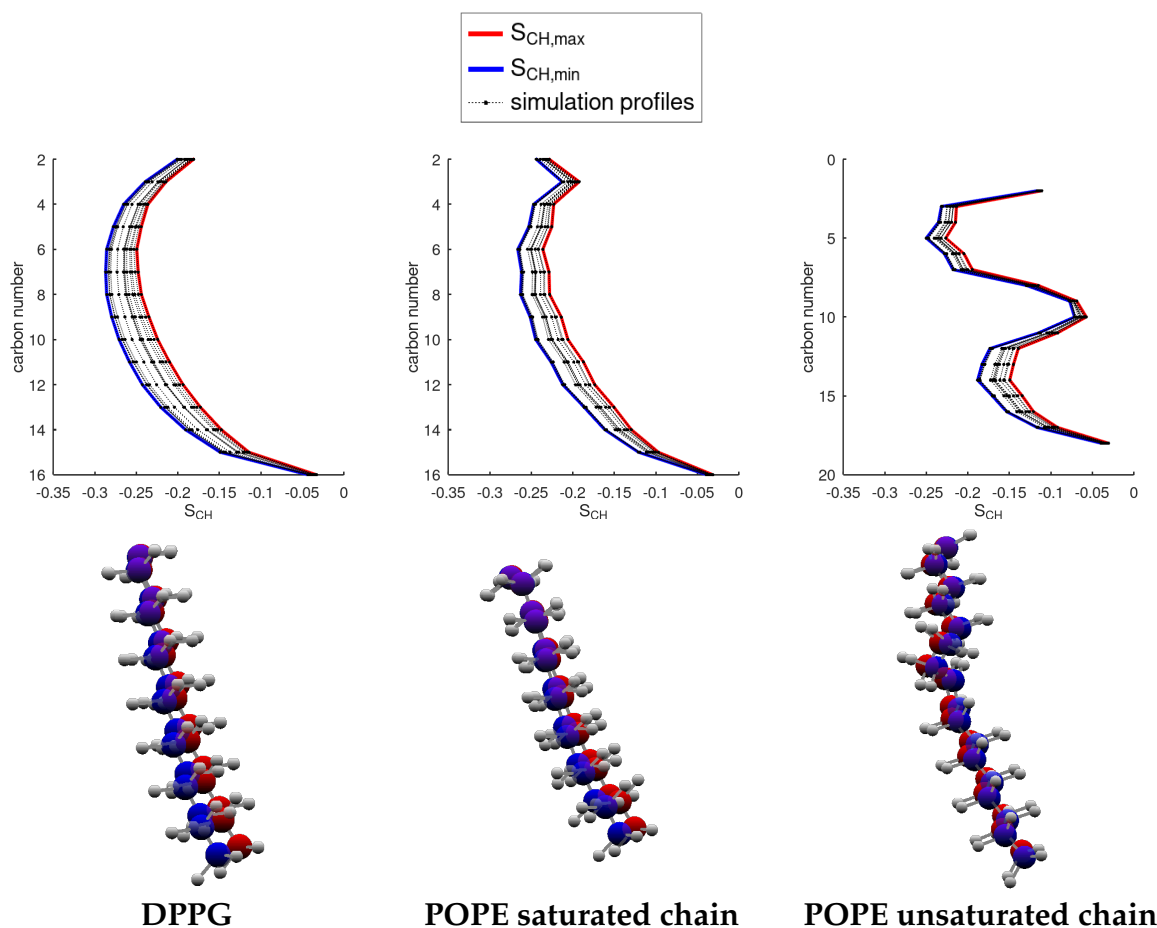


Figure 3.7: S_{CH} parameters for each simulation and respective lipid-tail illustration (the lipid tails coloured in blue and red represent the maximum and minimum S_{CH} profiles).

Since S_{CH} values for each lipid-tail carbon atom are highly correlated parameters, the principal component analysis (PCA) technique was adopted for the analysis of the S_{CH} data. The total 47 carbon lipid tail order parameters (15 for DPPG +17 for POPE unsaturated chain +15 for POPE saturated chain) were considered. The first principal component (PC1) accounted for 99 % of all variance, validating the methodology. The PC1 coefficients are represented in Figure B.1.

The PC1 scores were considered in the fitting of the linear regression model and the data are plotted in Figure 3.8 and summarized in Table 3.3. PC1 results were highly correlated to the thickness results ($r^2 = 0.985$), which is not surprising, since a straighter lipid tail orientation would result in a thicker membrane and vice-versa. Similarly to the thickness regression model, temperature has a clear effect on the lipid tail orientation (see b_T) and so does peptide concentration (see b_C), with a bit less statistical significance as shown by the parameter's p-values. Both contribute to a less vertically oriented lipid tail. The temperature-concentration interaction factor ($b_{T \times C}$) was not statistically significant (p-value=0.94).

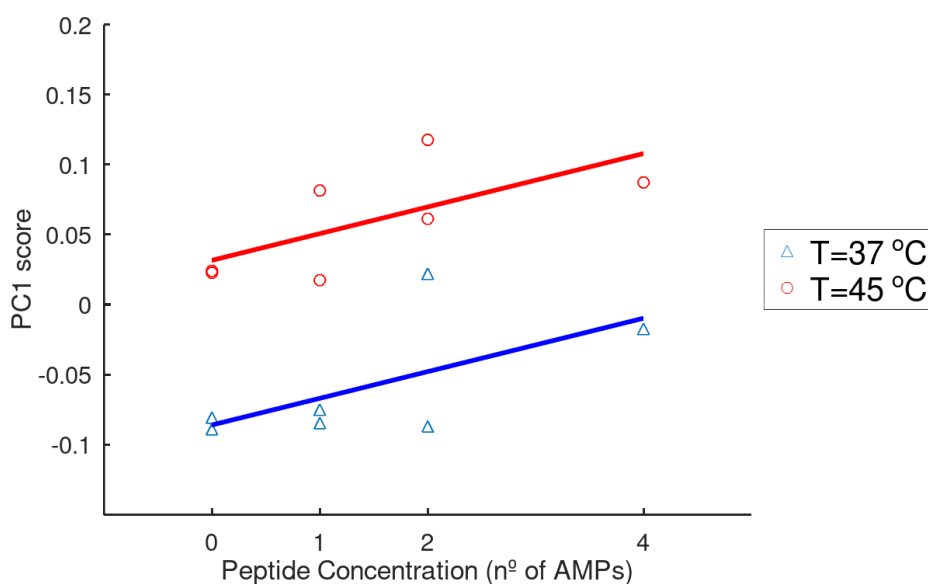


Figure 3.8: S_{CH} -PC1 linear regression model.

Table 3.3: Parameter estimation for the S_{CH} -PC1 regression model.

Model: $Y = a + b_T T + b_C C$			
Parameter	Estimate	Confidence Interval (95 %)	p-value ($\alpha = 0.05$)
a	-0.630	[-0.830, -0.430]	<0.001
b_T	0.0147	[0.0099, 0.0195]	<0.001
b_C	0.0191	[0.0041, 0.0340]	0.017

3.2.3 Lateral diffusion

The lipid diffusion coefficient can be estimated from the mean square displacement (MSD) of the lipid molecules, and by considering the Einstein's relation (Allen and Tildesley, 2017):

$$\lim_{t \rightarrow \infty} \langle \|r_i(t) - r_{i,0}\|^2 \rangle = 6D_A t \quad (3.3)$$

The MSD data for each simulation were obtained with the GROMACS analysis tool `gmx msd`, and the diffusion coefficients of both DPPG and POPE were estimated and fitted to a linear regression model. The data is plotted in Figure 3.9 and the parameter estimation summarized in Table 3.4. The first observation is that the lipid with an unsaturated chain (POPE) diffuses more easily than the one with all saturated chains (DPPG), due to overall higher diffusion coefficient values (see Figure 3.9). An increase in temperature has a clear positive effect on diffusion (see b_T), which is to be expected owing to the correspondingly higher thermal agitation. On the other hand, the peptide concentration has a negative effect on lipid diffusion (see $b_{T \times C}$), probably due to the overall attractive electrostatic forces between peptide and lipid. The resulting peptide-lipid hydrogen bonds inhibit overall lipid movement. This is a combined effect with temperature, which means it is reinforced by it. The peptide concentration (b_C) and intersect (a) parameters were not statistically significant.

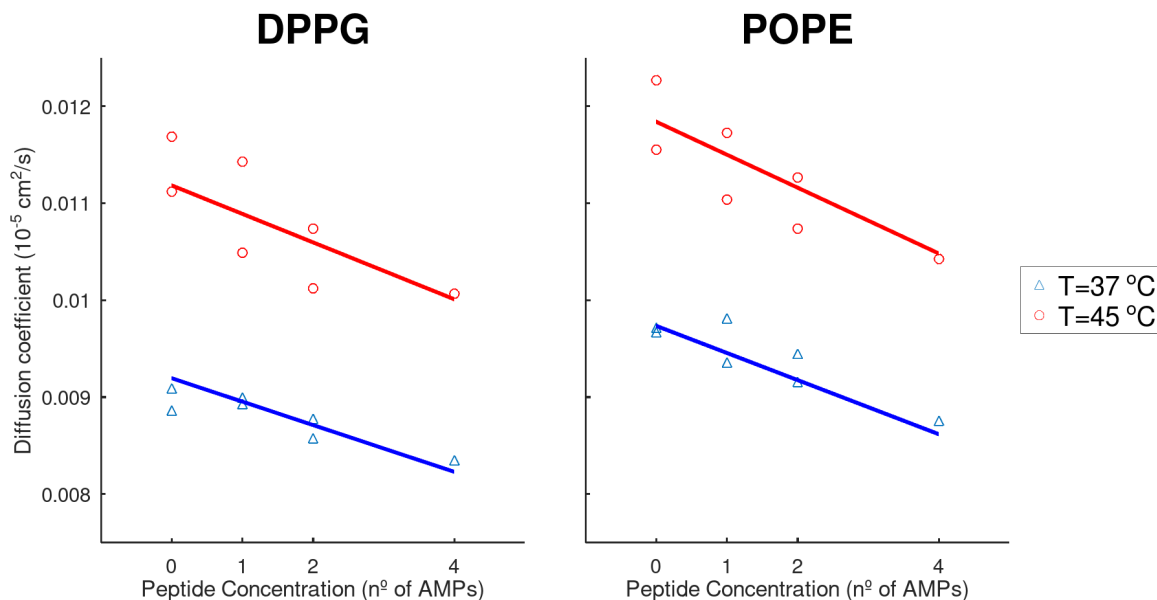


Figure 3.9: Diffusion coefficient linear regression models for both DPPG and POPE.

Table 3.4: Parameter estimation for the diffusion coefficient regression models.

DPPG Model: $Y = b_T T + b_{T \times C}(T \times C)$			
Parameter	Estimate	Confidence Interval (95 %)	p-value ($\alpha = 0.05$)
b_T	2.48e-04	[2.42e-04, 2.55e-04]	<0.001
$b_{T \times C}$	-6.52e-06	[-9.86e-06, -3.19e-06]	0.001
POPE Model: $Y = b_T T + b_{T \times C}(T \times C)$			
b_T	2.63e-04	[2.57e-04, 2.69e-04]	<0.001
$b_{T \times C}$	-7.55e-06	[-1.07e-05, -4.43e-06]	<0.001

3.2.4 Permeability

The membrane permeability was evaluated by the rate of transmembrane crossings of water molecules. The occurrence of these events was modelled as a homogeneous Poisson point process, which is based on the following assumptions:

- past occurrences do not affect the occurrence of future events, which means that they occur independently;
- the event occurrence rate (λ) is constant throughout the underlying Poisson point process space (time or spatial dimensions).

These properties mean that the distance between two consecutive points in an one-dimensional space is described by an exponential distribution with constant $1/\lambda$. The histograms for the inter-event time distribution of each simulation, as well as the P-P plots for the fitting with an exponential distribution (shown in Figure B.2 and Figure B.3, Appendix) appear to comply with the assumptions above.

The number of events was counted for each simulation, as shown in Figure 3.10. The event occurrence rate (λ) and its standard deviation (σ_λ) were estimated based on the total number of events (μ) and the simulation time (t), as described in Equation 3.4 and Equation 3.5 respectively.

$$\lambda = \frac{\mu}{t} \quad (3.4)$$

$$\sigma_\lambda = \sqrt{\frac{\lambda}{t}} \quad (3.5)$$

the results of which are shown in Figure 3.11.

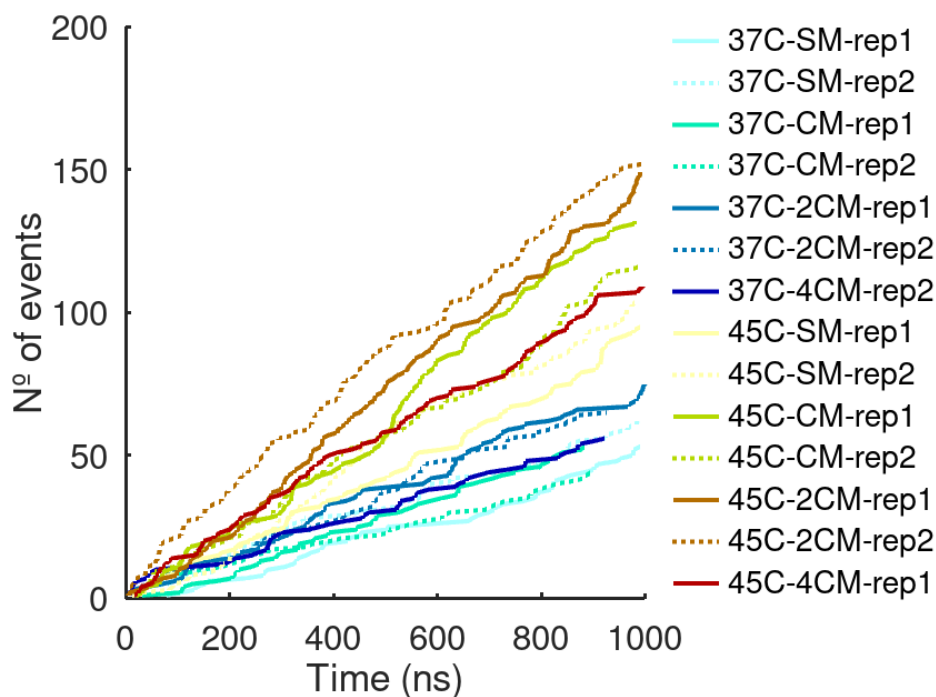


Figure 3.10: Counting of transmembrane crossings of water molecules throughout the simulation times.

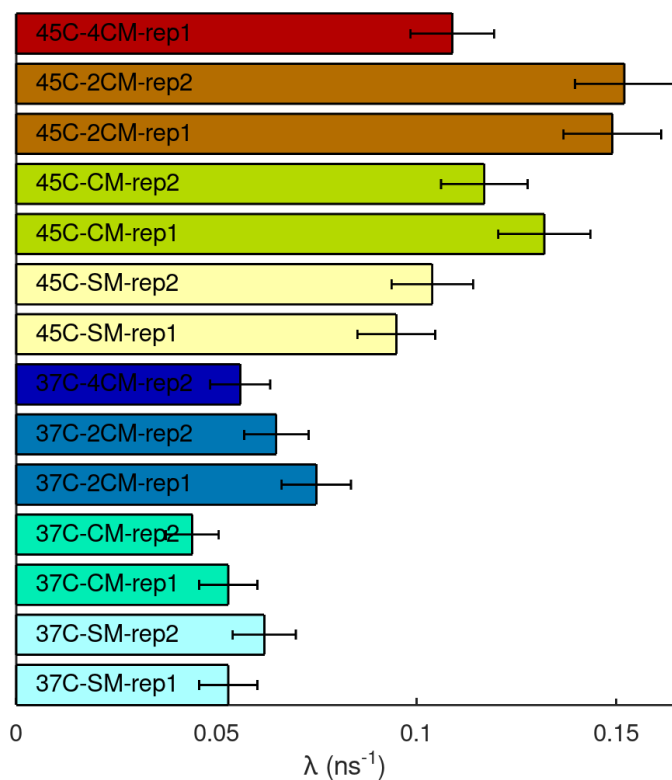


Figure 3.11: Rate of transmembrane crossings of water molecules (λ) and its estimated standard deviation (represented with error bars) for each simulation.

A linear regression model was fitted to the occurrence rate data considering the rate estimation variance. This is achieved by using weights for each data point inversely proportional to the data point's variance ($\frac{1}{w_i} \propto \sigma_{\lambda_i}^2$). This method is called Weighted Least Squares regression (Strutz, 2016). The data are plotted in Figure 3.12 and the parameter estimation summarized in Table 3.5.

The peptide concentration effect is not statistically significant (p-value = 0.364), mainly due to the non-linear effect of peptide concentration. For simulations with 4 AMPs, the permeability drops significantly. This likely happens because the peptides, at this concentration, cover a large portion of membrane surface, lowering the total water-membrane interface area and preventing the passage of water molecules through the membrane. If the 4-peptide concentration simulations are not considered (Model 2), the concentration-temperature combined effect parameter does seem to have a positive impact on permeability, although not enough to rule out the null hypothesis.

Temperature is shown to have a major effect on membrane permeability (see b_T). In Model 1, the event occurrence rate more than doubles ($\lambda_{45^\circ\text{C}} / \lambda_{37^\circ\text{C}} \approx 2.1$) with an 8°C temperature increase.

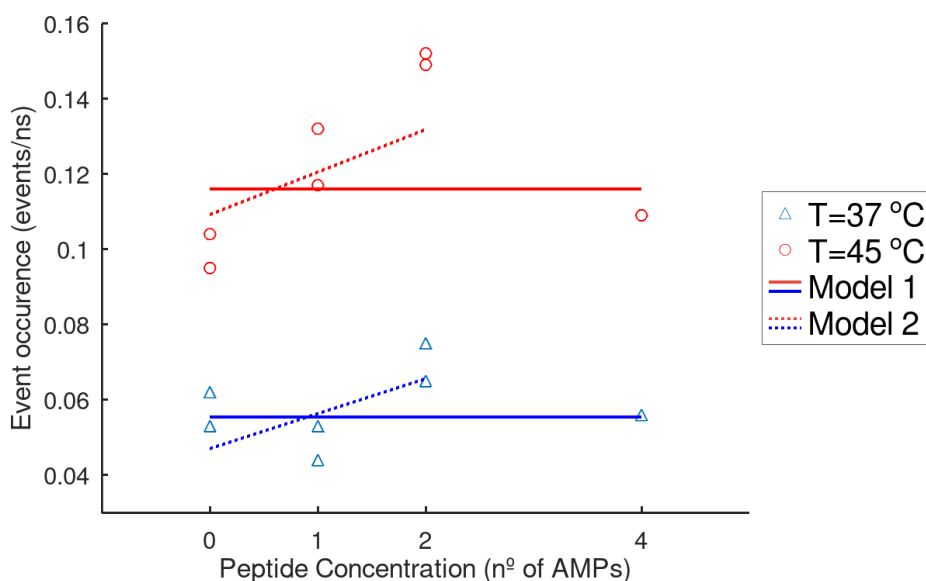


Figure 3.12: Membrane permeability linear regression.

Table 3.5: Parameter estimation for the membrane permeability regression models.

Model 1: $Y = a + b_T T$			
Parameter	Estimate	Confidence Interval (95 %)	p-value ($\alpha = 0.05$)
a	-0.248	[-0.314, -0.135]	<0.001
b_T	7.57e-03	[5.25e-03, 9.89e-03]	<0.001
Model 2: $Y = a + b_T T + b_C C + b_{T \times C}(T \times C)$			
a	-0.241	[-0.335, -0.146]	<0.001
b_T	7.77e-03	[5.32e-03, 1.02e-02]	<0.001
$b_{T \times C}$	2.51e-04	[-1.24e-05, 5.15e-04]	0.059

3.2.5 Area per lipid

The area per lipid (APL) of each lipid molecule in its leaflet was calculated throughout the simulation times as described in section 2.3. Figure 3.13 illustrates the membrane's upper leaflet in simulation "45C-CM-rep1" at different time points.

In the initial stage of the simulation ($t < 50$ ns), the LL37-PEG conjugate is still on top of the membrane without interfering with the phospholipids. After that, the peptide penetrates the membrane resulting in the displacement of some lipids, leading them to virtually occupy a larger surface area.

This phenomenon also occurs in other simulations, as shown in Figure 3.14, which includes the APL average and the 98th percentile statistic for both lipids (DPPG and POPE) throughout the simulation time. The APL for some lipids reached values ≈ 2.13 times higher than the system's average, as in the case of the "45C-CM-rep1" simulation. The average APL values appeared to remain unchanged.

To evaluate the effect of the peptide and concentration on the average APL for both lipids, a regression model was fitted for each lipid (see Figure 3.15 and Table 3.6). As expected, the effect of temperature is very noticeable, resulting in an increase of membrane area of about 3.8 % (DPPG) and 3.4 % (POPE) for a temperature increase of 8°C. Peptide concentration has a combined effect with temperature, specifically regarding the DPPG molecules. Since DPPG has a net-negative charge, the positively charged peptide tends to interact more with it than with the POPE. The latter also seems to be affected by the peptide, but the null hypothesis could not be ruled out.

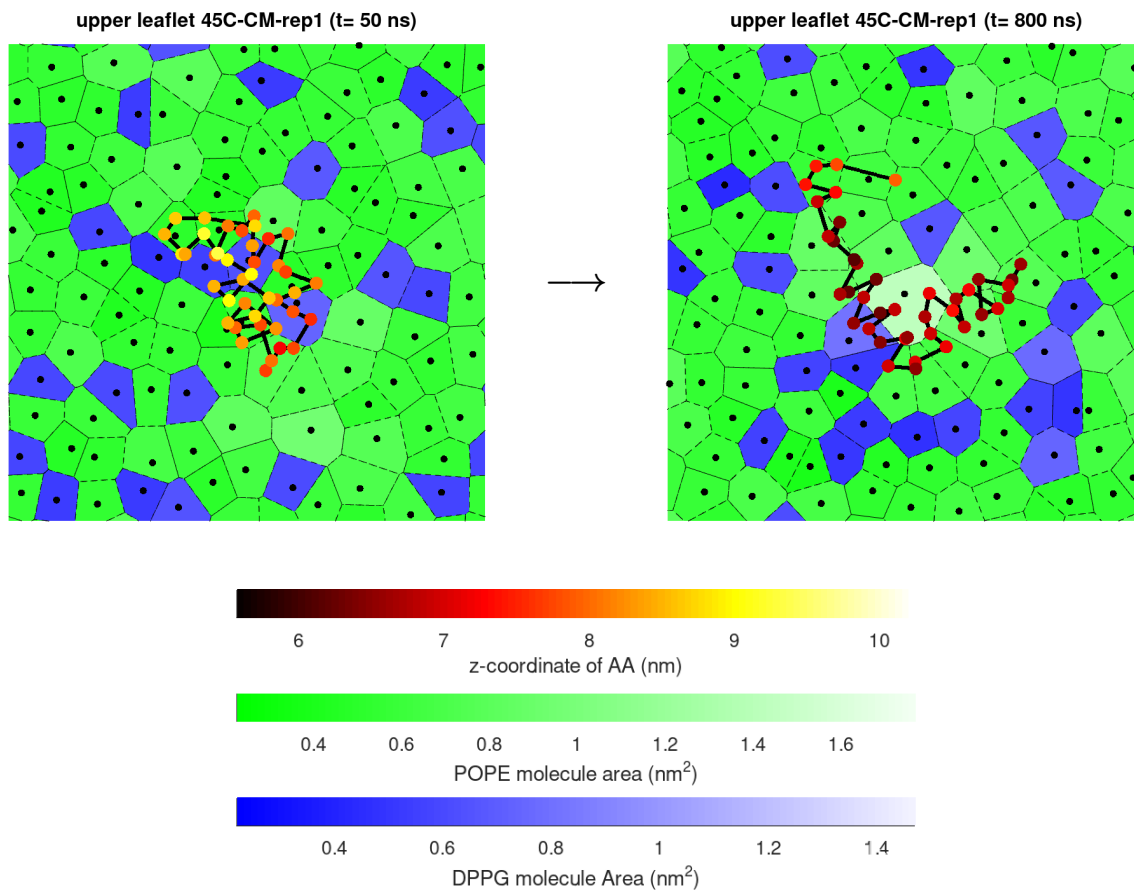


Figure 3.13: Representation of the phospholipid positioning and respective area for the "45-CM-rep1" simulation at two time points ($t = 50$ ns and $t = 800$ ns); The LL37-PEG position is represented through the COM of the amino acids (z-coordinate is represented with colour).

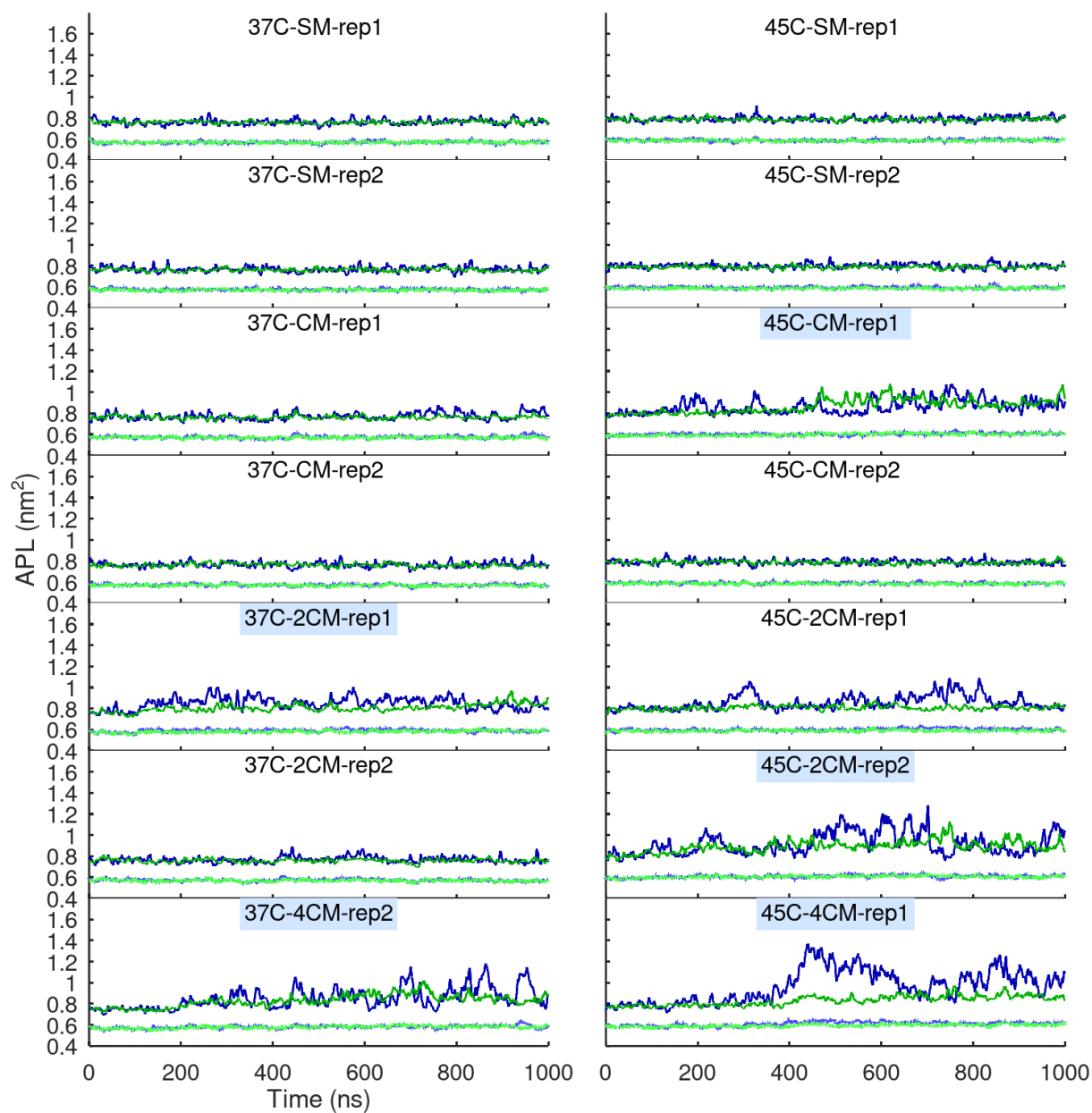


Figure 3.14: Average membrane area per lipid (APL) vs 98th percentile (DPPG: average —, 98th percentile —; POPE: average —, 98th percentile —; Simulations with membrane penetration: ■).

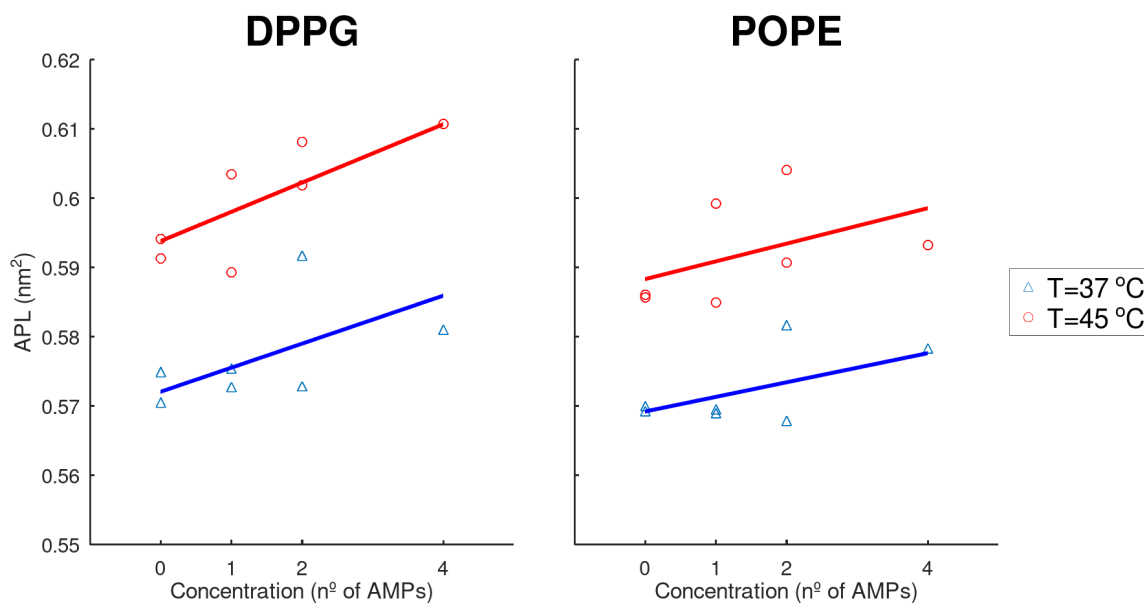


Figure 3.15: APL linear regression models for both DPPG and POPE.

Table 3.6: Parameter estimation for the APL regression models.

DPPG Model: $Y = a + b_T T + b_{T \times C}(T \times C)$			
Parameter	Estimate	Confidence Interval (95 %)	p-value ($\alpha = 0.05$)
a	0.472	[0.435, 0.508]	<0.001
b_T	2.72e-03	[1.84e-03, 3.60e-03]	<0.001
$b_{T \times C}$	9.37e-05	[2.80e-05, 1.59e-04]	0.009
POPE Model: $Y = a + b_T T + b_{T \times C}(T \times C)$			
a	0.481	[0.446, 0.516]	<0.001
b_T	2.39e-03	[1.53e-03, 3.25e-03]	<0.001
$b_{T \times C}$	5.69e-05	[-7.48e-06, 1.21e-04]	0.078

3.2.6 Hydrogen bonds

The formation of H-bonds between phospholipid molecules was studied based on data obtained through the GROMACS analysis tool `gmx hbond`. Phospholipids can only form H-bonds via their head groups. The specific donor or acceptor of hydrogen atoms for both DPPG and POPE are highlighted in Figure 3.16.

For each simulation, the H-bonds between separate lipid molecules were counted and categorized based on the acceptor and donor atoms. The data regarding the average number of bonds for each bond category ("Donor-Acceptor"), considering all simulations, is plotted in Figure 3.17. The favored acceptor atoms are clearly the "O2L" elements of the phosphate group of both DPPG and POPE, presumably due to its high

negative charge. The "OBL" and "OSLP" atoms are the next favored atoms.

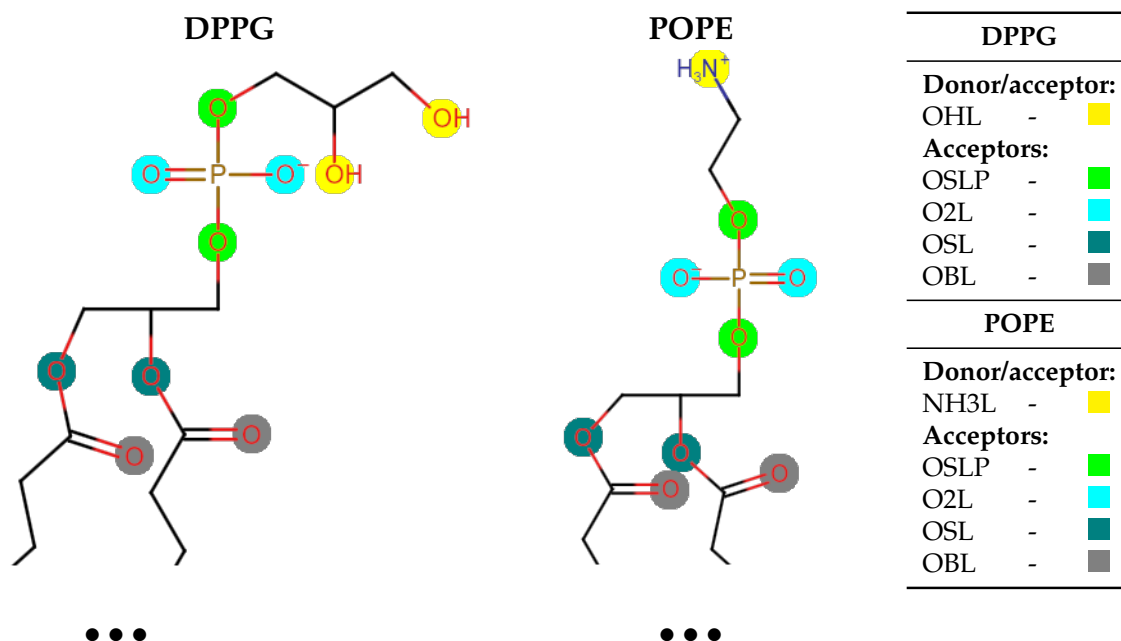


Figure 3.16: Representation and labelling of the hydrogen donor and acceptor atoms of the phospholipid heads of DPPG and POPE.

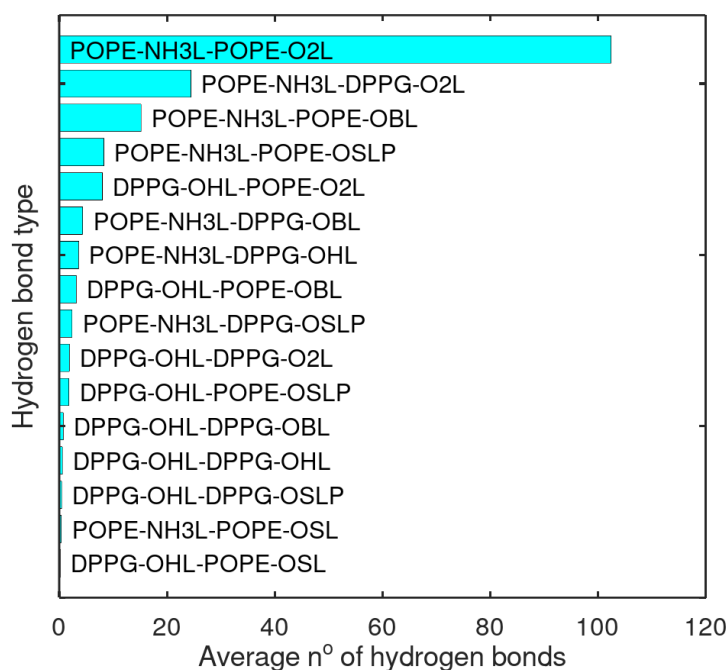


Figure 3.17: Average number of hydrogen bonds between each donor and acceptor atom.

The data on the average number of H-bonds considering all categories was used for the fitting of the linear regression model. The data is plotted in Figure 3.18 and the parameter estimation summarized in Table 3.7. Peptide concentration does not seem

to influence the number of H-bonds. On the other hand, the increase in temperature contributes to a decrease of about 3.3 % (≈ -6.06 bonds) in the average number of H-bonds, likely due to a higher mobility of the phospholipids.

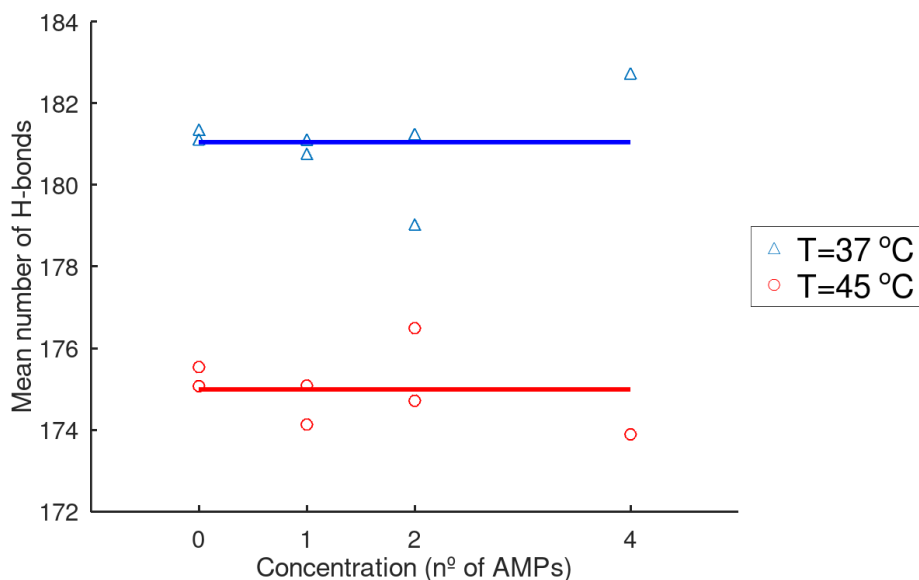


Figure 3.18: Linear regression model for the number of hydrogen bonds between membrane molecules.

Table 3.7: Parameter estimation for the regression model of the number of hydrogen bonds between membrane molecules.

Model: $Y = a + b_T T$			
Parameter	Estimate	Confidence Interval (95 %)	p-value ($\alpha = 0.05$)
a	209.1	[203.1, 215.0]	<0.001
b_T	-0.758	[-0.901, -0.614]	<0.001

3.3 Peptide-membrane interaction

In this section, an in-depth analysis of the interaction between the peptide and the membrane is reported. Several features are analyzed to better understand the mechanism of action of the peptide, such as the positioning of the LL37-PEG conjugate on the membrane and the formation of H-bonds.

3.3.1 Positioning and Forces

The z-coordinate of each LL37 amino acid was averaged for the last 500 ns of each simulation. The time intervals where membrane penetration was observed were accounted separately. The data are plotted in Figure 3.19. The first observation is that the last part of peptide (residues 31-38) is positioned away from the membrane, meaning that it was never really adsorbed to the surface. Therefore, both the linker (MAL) and the oligomer (PEG), which are considered in residue "38CYL", do not seem to interact with the membrane.

The amphipathic structure of the peptide is shown to have a remarkable influence on the positioning of the peptide as it penetrates the membrane. The hydrophobic amino acids stuck into the deeper parts of the membrane, likely interacting with its hydrophobic part. On the other hand, the hydrophilic amino acids stood on the membrane's surface, i.e. near phosphate groups. As shown in the "no membrane penetration" representation of Figure 3.19, the amphipathic configuration is established as the peptides dig deeper in the membrane. Anyway, the peptides still laid parallel to the membrane similarly to the Carpet model.

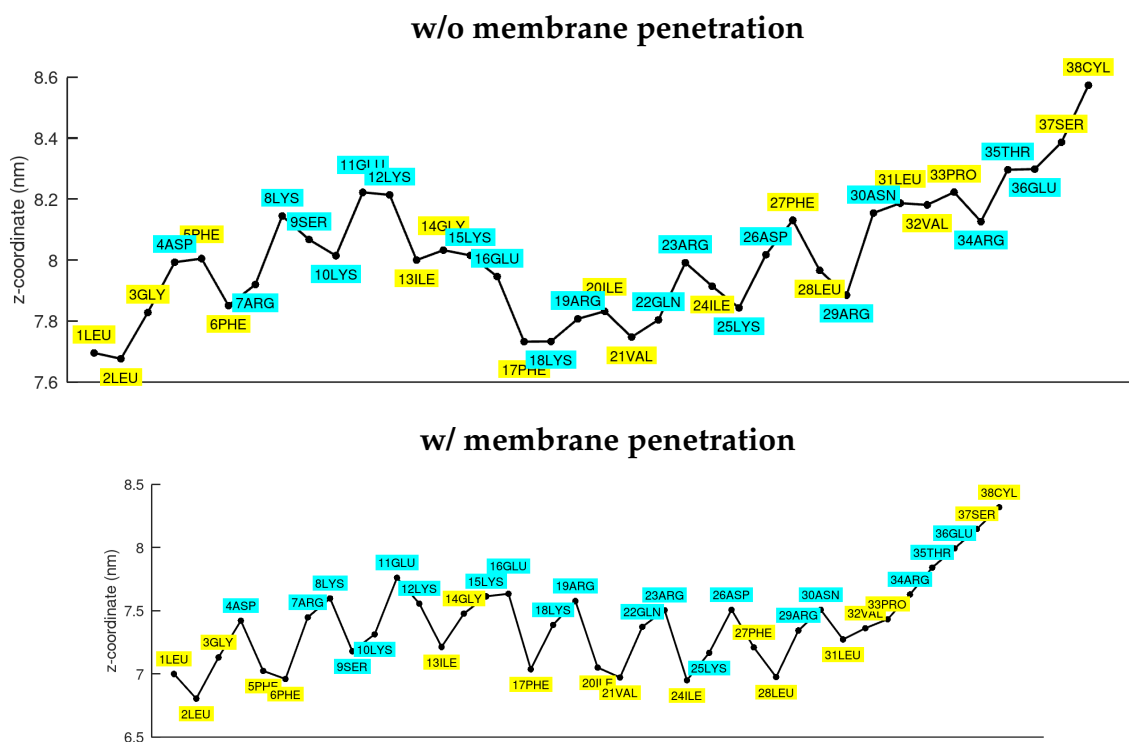


Figure 3.19: Average z-coordinate of each amino acid over all peptides in the last 500 ns of all simulations (Hydrophobic amino acids: ■; Hydrophilic amino acids: ■).

The forces exerted on the peptides by the membrane were calculated using the simulation (rerun) feature of GROMACS. Each simulation was rerun considering only the

peptide and also considering the membrane+peptide together. Equation 3.6 was used to compute the forces exerted by the membrane.

$$F_{\text{mem}} = F_{\text{mem+pep}} - F_{\text{pep}} \quad (3.6)$$

The average z -force acting on each amino acid in the last 200 ns of simulation is shown in Figure 3.20. Unsurprisingly, the peptide is generally attracted to the membrane in segments where positively charged amino acids prevail, while the opposite is true for negatively charged amino acids. Even so, despite the net-negative charge of "36GLU" and "38CYL", they do not seem to interact with the membrane, likely due to them being at the end part of the peptide, which is kept away from the membrane surface.

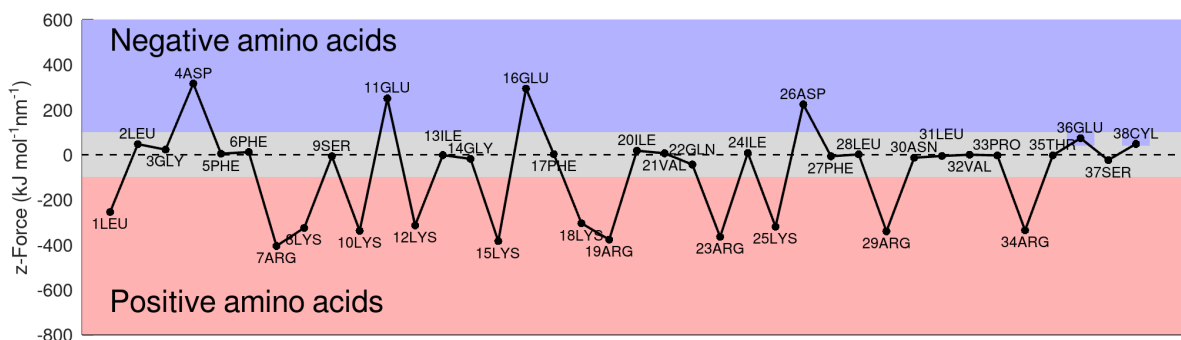


Figure 3.20: Average z -force exerted on each amino acid by the membrane (negative force values mean attractive forces).

3.3.2 Hydrogen bonds

In the same way as in subsection 3.2.6, the number of H-bonds was calculated for the peptide-membrane interactions and within the peptide. In the case of peptide-membrane H-bonds, the average number of bonds throughout the simulation was computed for each acceptor/donor atom of the LL37-PEG conjugate. The data are plotted in Figure 3.21 and Figure 3.22. The main hydrogen donors are located in the positively charged side chains of the arginine (ARG) and lysine (LYS) residues. The peptide terminal groups NH_3^+ and COO^- also bonded to the membrane, mainly the positive NH_3^+ moiety. The negatively charged side of the Aspartic acid (ASP) and of the glutamic acid (GLU) bonded to membrane as hydrogen acceptors. The atoms of peptide backbone did not bond to the membrane.

The effect of temperature on the bonding of specific peptide atoms with the membrane could not be studied because each specific peptide bonded differently with the

membrane depending on the simulation. For a more comprehensive study on the specific H-bonding sites of the peptide, a larger number of simulations with different initial configurations would be necessary to correctly sample this phenomenon with such a level of detail.

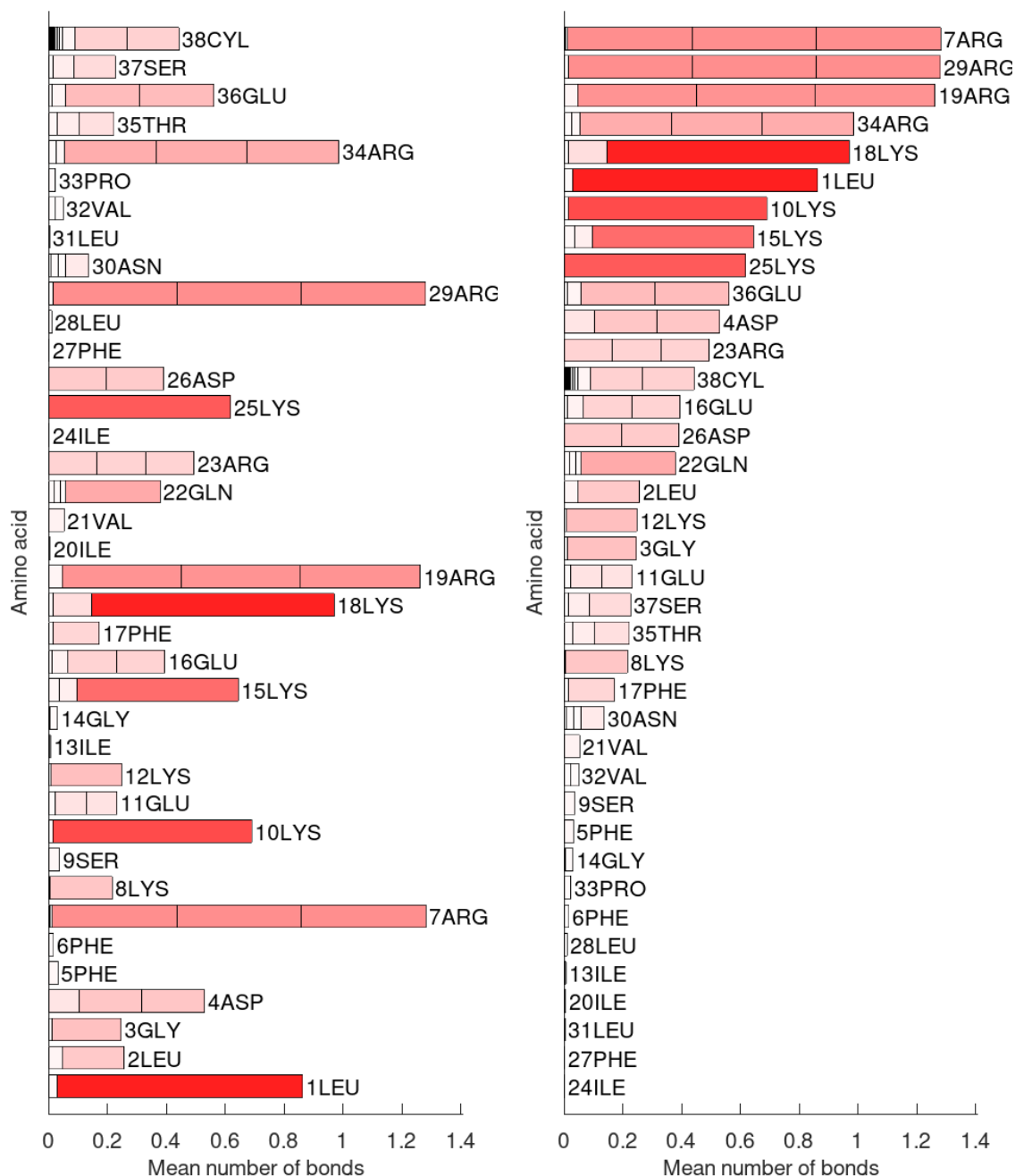


Figure 3.21: Mean number of hydrogen bonds formed between each amino acid and the membrane, by residue order (left) and by descending order of the mean number of bonds (right).

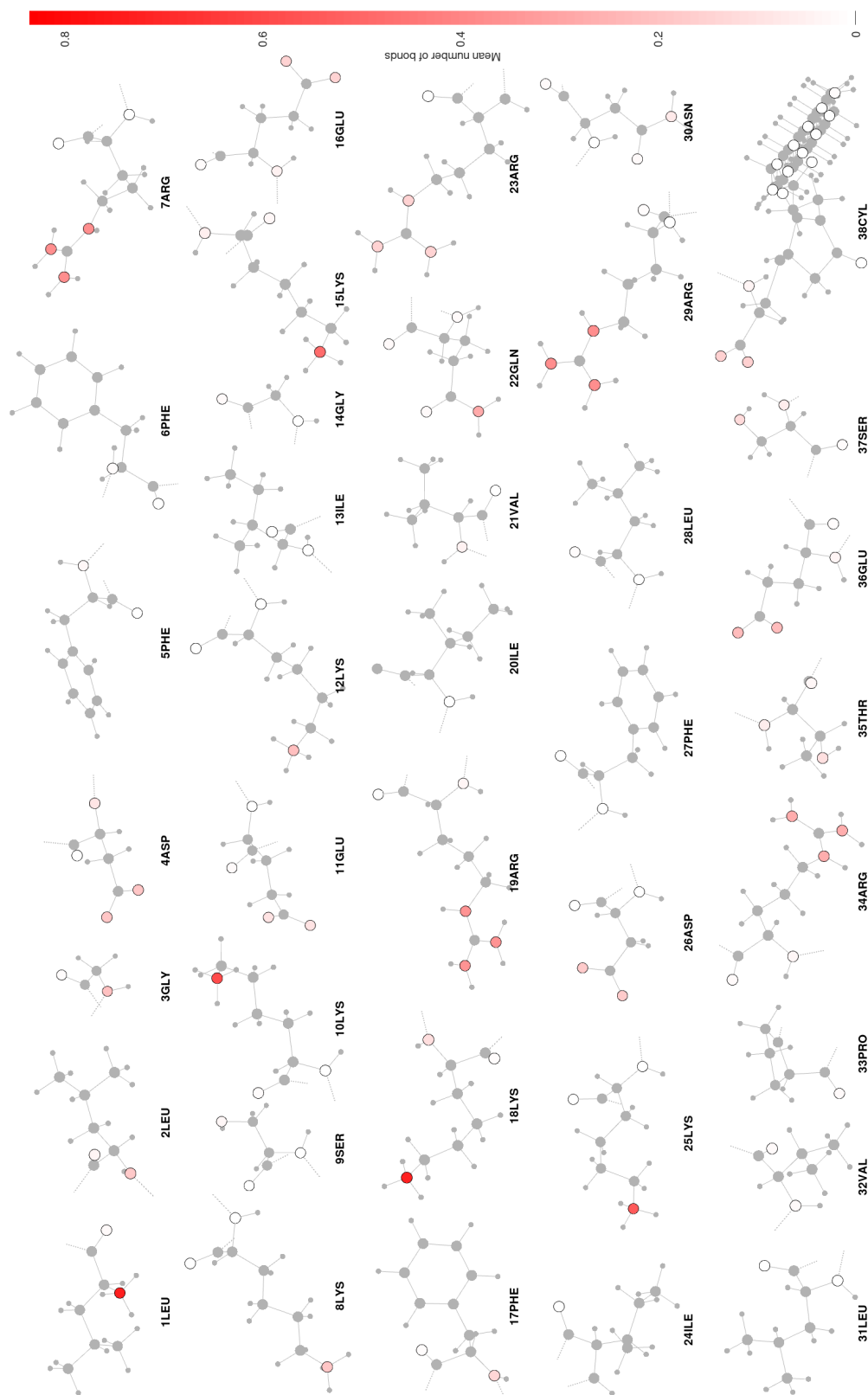


Figure 3.22: Representation of both donor and acceptor atoms for each residue of the peptide, and respective average number of hydrogen bonds formed with the membrane. The average number of bonds is calculated considering all the peptides from all the simulations.

The analysis of the number of H-bonds within the peptide was carried out mainly to study the α -helix structure of peptide and how it was affected when in contact with the bacterial membrane. The resulting data from the main simulations were compared to data from the additional peptide-only simulations. Figure 3.23 shows the information within a representation of the LL37-PEG conjugate.

The peptide exhibits two main α -helix sections involving the residues 1-14 and 16-31. When the peptide was in contact with the membrane, the average number of H-bonds forming these α -helix sections was increased. This suggests that the membrane might contribute to the maintenance of this amphipathic structure of the peptide. At 45°C, the number of bonds in the α -helices is slightly higher than at a lower temperature, suggesting that the peptide can more easily arrange itself in a more fluid membrane.

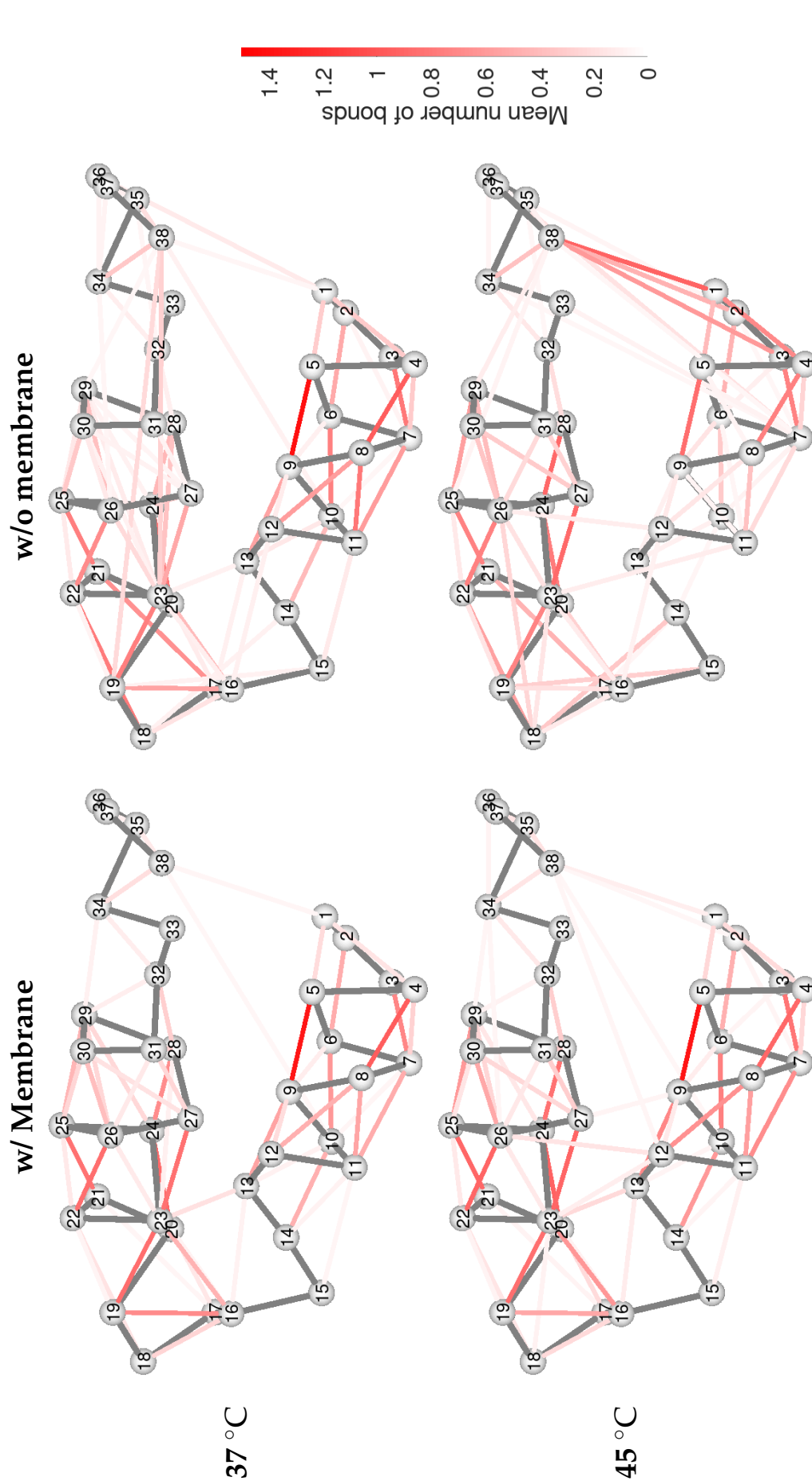


Figure 3.23: Representation of the LL37-PEG and average number of intra-peptide hydrogen bonds for simulations with and without a membrane.

3.3.3 Ion displacement

A consequence of the interaction of a cationic AMP with the membrane is the displacement of positively charged ions, in this case the potassium ion (K^+). Figure 3.24 shows the density profiles obtained using the GROMACS analysis tool `gmx density`, while Figure 3.25 shows a 2D density map regarding K^+ ion concentration on the upper surface of the bilayer. Both figures demonstrate the ion displacement phenomenon. In the no-peptide simulations the amount of ions is the same on both sides of the membrane, whereas with the presence of peptide, the ions diffused mostly to the opposite surface of the membrane. This effect is also seen locally on the upper surface of the membrane, as the number of K^+ ions positioned near the peptide is by far lower than in the rest of the simulation box.

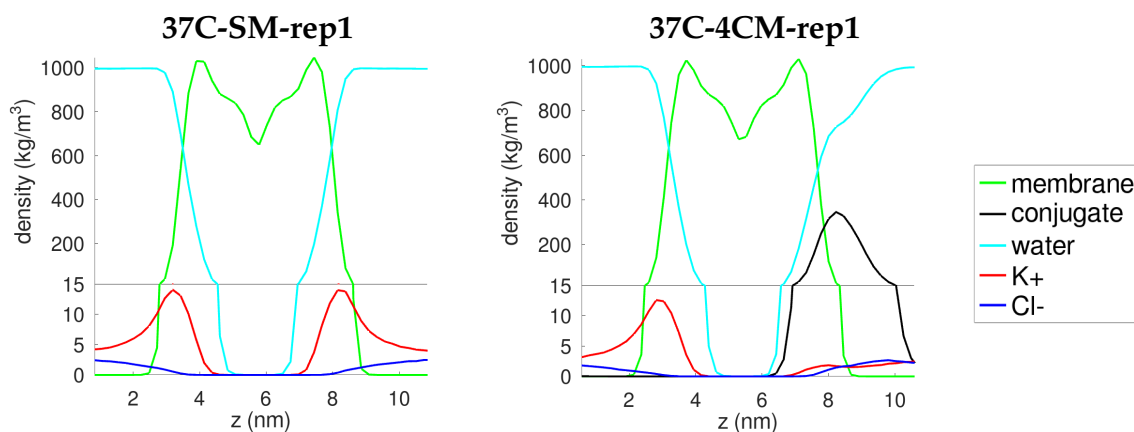


Figure 3.24: Density profiles for each system component.

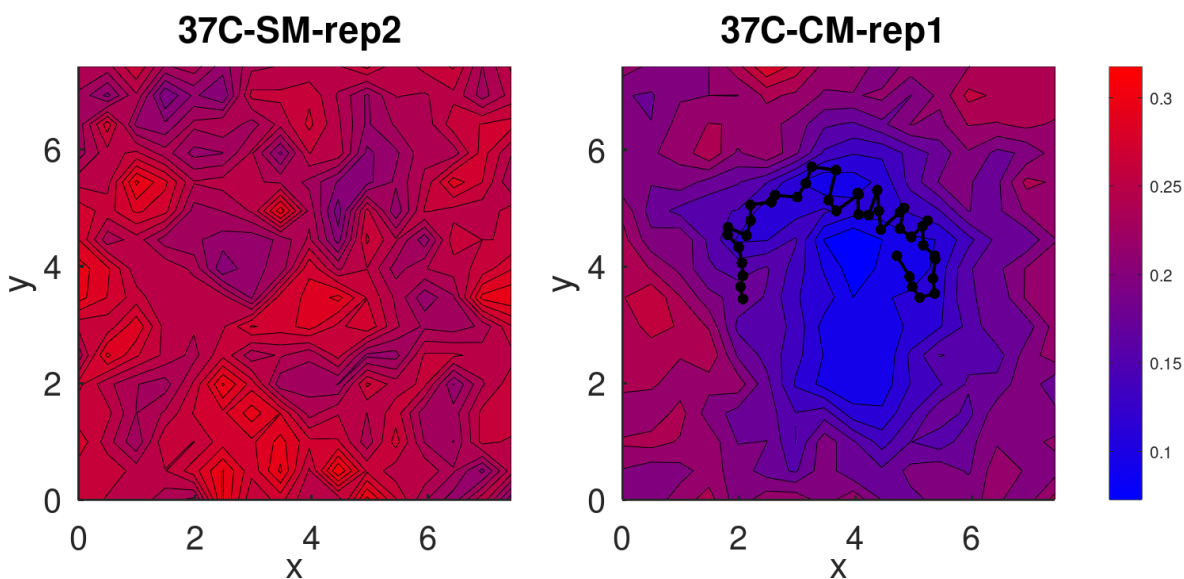


Figure 3.25: Potassium ion concentration color map (peptide: —).

3.4 Discussion

This study evaluated the interaction between the LL37-PEG conjugate and membrane, and the effect of temperature and peptide concentration on membrane properties. The peptide was shown to be rapidly attracted by the membrane, and as it interacted with it, it would arrange itself in the α -helix structure. This happened specifically in some peptide sections: residues 1-14 and 16-31. The amphipathic nature of the structure was critical to the insertion of the peptide into the membrane, as the hydrophobic amino acids residues were placed near the hydrophobic lipid tails of the membrane, and the hydrophilic residues bonded with phospholipid heads at the surface level. The positively charged residues (arginine and lysine) were shown to have great importance in forming H-bonds with both the membrane's lipids (DPPG and POPE). The C-terminal section of peptide (residues 31-38) was shown to not interact greatly with the membrane, making it suitable for the fixation on the implant material surface.

The peptide affected the membrane in various ways. The peptide insertion in the membrane caused some local displacement of the lipid molecules, and consequently the membrane thickness decreased locally. The formation of bonds with the phospholipid caused a local decrease in membrane fluidity, suggested by lower lateral diffusion coefficients. No consistent effect on membrane permeability was recorded, though this does not mean that the membrane permeability is not affected by the presence of peptide. At a larger timescale, with the eventual formation of more-established peptide-membrane structures such as pores, the membrane permeability could be affected. The ion displacement phenomenon is also a very important mechanism of action, as the removal of positive ions can affect several membrane structures, compromising their ability to carry out their normal functions.

The system's temperature had an effect on every single evaluated membrane property. An increase of 8 °C caused a decrease in membrane thickness, and increases in membrane fluidity and APL. Perhaps the most interesting effect of temperature was the increase in membrane permeability. Just as small molecules such as water can more easily access the membrane, larger solutes such as peptides can insert themselves into the membrane with less difficulty. This is in agreement with the observed membrane penetration data, as in the 45 °C simulations, the total recorded time of peptide insertion was longer than in the other simulations. The increased membrane fluidity would also help towards more easily establishing the peptide's amphipathic structure.

The analyzed data suggests that the combined use of AMP-coated materials in conjunction with photothermal therapy may be a viable strategy for the prevention of bacterial infection.

4. Conclusions and future perspectives

This study uses an MD simulation approach to study both the antimicrobial mechanism of action of the LL37 peptide, as well as the effect of temperature on the interaction, for application in dental implant systems. A total of fourteen 1- μ s simulations were carried out considering a bacterial mimetic model membrane and the peptide conjugated with PEG at various concentrations. The photothermal effect was considered by increasing the system's temperature from 37 °C to 45 °C in some simulations.

The acquired data show that the peptide slowly arranges itself in an α -helix structure when adhered to the bacterial membrane, having the hydrophobic residues facing the inside of the membrane. The increase in temperature had a very noticeable effect on the membrane properties, contributing mainly to a thinner and more fluid membrane. This allowed the peptide to more easily insert itself in the membrane.

Future studies on the mechanism of AMPs for the application in dental implant systems could include:

- the study of the combined effect of different AMPs to investigate eventual synergistic interactions;
- the use of advanced sampling methods, such as Metadynamics, for the free-energy investigation of peptide-membrane interaction;
- the study of the peptide-membrane interaction at longer timescales using Coarse-Grained simulations.

References

- Allen, M. P. and Tildesley, D. J. (2017). *Computer Simulation of Liquids*. Oxford University Press.
- Andersen, H. C. (2008). Molecular dynamics simulations at constant pressure and/or temperature. *The Journal of Chemical Physics*, 72(4):2384–2393.
- Bernetti, M. and Bussi, G. (2020). Pressure control using stochastic cell rescaling. *The Journal of Chemical Physics*, 153(11):114107.
- Blender Online Community (2018). *Blender - a 3D modelling and rendering package*. Blender Foundation, Stichting Blender Foundation, Amsterdam.
- Bussi, G., Donadio, D., and Parrinello, M. (2007). Canonical sampling through velocity rescaling. *The Journal of Chemical Physics*, 126(1):014101.
- Chakraborty, A., Kobzev, E., Chan, J., de Zoysa, G. H., Sarojini, V., Piggot, T. J., and Allison, J. R. (2020). Molecular dynamics simulation of the interaction of two linear battacin analogs with model gram-positive and gram-negative bacterial cell membranes. *ACS Omega*, 6(1):388–400.
- Duay, S. S., Sharma, G., Prabhakar, R., Angeles-Boza, A. M., and May, E. R. (2019). Molecular dynamics investigation into the effect of zinc(II) on the structure and membrane interactions of the antimicrobial peptide clavanin a. *The Journal of Physical Chemistry B*, 123(15):3163–3176.
- Gan, B. H., Gaynord, J., Rowe, S. M., Deingruber, T., and Spring, D. R. (2021). The multifaceted nature of antimicrobial peptides: current synthetic chemistry approaches and future directions. *Chemical Society Reviews*, 50(13):7820–7880.
- Hoover (1985). Canonical dynamics: Equilibrium phase-space distributions. *Physical review. A, General physics*, 31 3:1695–1697.
- Huan, Y., Kong, Q., Mou, H., and Yi, H. (2020). Antimicrobial peptides: Classification, design, application and research progress in multiple fields. *Frontiers in Microbiology*, 11.

- Huang, J., Rauscher, S., Nawrocki, G., Ran, T., Feig, M., de Groot, B. L., Grubmüller, H., and MacKerell, A. D. (2016). CHARMM36m: an improved force field for folded and intrinsically disordered proteins. *Nature Methods*, 14(1):71–73.
- Jo, S., Kim, T., Iyer, V. G., and Im, W. (2008). CHARMM-GUI: A web-based graphical user interface for CHARMM. *Journal of Computational Chemistry*, 29(11):1859–1865.
- Jo, S., Lim, J. B., Klauda, J. B., and Im, W. (2009). CHARMM-GUI membrane builder for mixed bilayers and its application to yeast membranes. *Biophysical Journal*, 97(1):50–58.
- Kim, S., Lee, J., Jo, S., Brooks, C. L., Lee, H. S., and Im, W. (2017). CHARMM-GUI ligand reader and modeler for CHARMM force field generation of small molecules. *Journal of Computational Chemistry*, 38(21):1879–1886.
- Kittaka, M., Shiba, H., Kajiya, M., Fujita, T., Iwata, T., Rathvisal, K., Ouhara, K., Takeda, K., Fujita, T., Komatsuzawa, H., and Kurihara, H. (2013). The antimicrobial peptide LL37 promotes bone regeneration in a rat calvarial bone defect. *Peptides*, 46:136–142.
- Klauda, J. B., Venable, R. M., Freites, J. A., O'Connor, J. W., Tobias, D. J., Mondragon-Ramirez, C., Vorobyov, I., MacKerell, A. D. J., and Pastor, R. W. (2010). Update of the charmm all-atom additive force field for lipids: Validation on six lipid types. *The Journal of Physical Chemistry B*, 114(23):7830–7843. PMID: 20496934.
- Kormas, I., Pedercini, C., Pedercini, A., Raptopoulos, M., Alassy, H., and Wolff, L. F. (2020). Peri-implant diseases: Diagnosis, clinical, histological, microbiological characteristics and treatment strategies. a narrative review. *Antibiotics*, 9(11):835.
- Kumar, P., Kizhakkedathu, J., and Straus, S. (2018). Antimicrobial peptides: Diversity, mechanism of action and strategies to improve the activity and biocompatibility in vivo. *Biomolecules*, 8(1):4.
- Lai, Y. and Gallo, R. L. (2009). AMPed up immunity: how antimicrobial peptides have multiple roles in immune defense. *Trends in Immunology*, 30(3):131–141.
- Lee, C.-T., Huang, Y.-W., Zhu, L., and Weltman, R. (2017). Prevalences of peri-implantitis and peri-implant mucositis: systematic review and meta-analysis. *Journal of Dentistry*, 62:1–12.
- Nijnik, A. and Hancock, R. (2009). Host defence peptides: antimicrobial and immunomodulatory activity and potential applications for tackling antibiotic-resistant infections. *Emerging Health Threats Journal*, 2(1):7078.

- Nosek, T. (1998). *Essentials of Human Physiology*. Gold Standard Multimedia Inc.
- Nosé, S. (1984). A molecular dynamics method for simulations in the canonical ensemble. *Molecular Physics*, 52(2):255–268.
- Ocampo-Ibáñez, I. D., Liscano, Y., Rivera-Sánchez, S. P., Oñate-Garzón, J., Lugo-Guevara, A. D., Flórez-Elvira, L. J., and Lesmes, M. C. (2020). A novel cecropin d-derived short cationic antimicrobial peptide exhibits antibacterial activity against wild-type and multidrug-resistant strains of *Klebsiella pneumoniae* and *Pseudomonas aeruginosa*. *Evolutionary Bioinformatics*, 16:117693432093626.
- Oren, Z. and Shai, Y. (1998). Mode of action of linear amphipathic α -helical antimicrobial peptides. *Biopolymers*, 47(6):451–463.
- Parihar, A., Singh, R., Vaibhav, V., Kumar, K., Singh, R., and Jerry, J. (2020). A 10 years retrospective study of assessment of prevalence and risk factors of dental implants failures. *Journal of Family Medicine and Primary Care*, 9(3):1617.
- Parrinello, M. and Rahman, A. (1981). Polymorphic transitions in single crystals: A new molecular dynamics method. *Journal of Applied Physics*, 52(12):7182–7190.
- Piggot, T. J., Allison, J. R., Sessions, R. B., and Essex, J. W. (2017). On the calculation of acyl chain order parameters from lipid simulations. *Journal of Chemical Theory and Computation*, 13(11):5683–5696.
- Resnik, R. (2019). *Misch's Contemporary Implant Dentistry*. Elsevier - Health Sciences Division.
- Ridyard, K. E. and Overhage, J. (2021). The potential of human peptide LL-37 as an antimicrobial and anti-biofilm agent. *Antibiotics*, 10(6):650.
- Sam, G. (2014). Evolution of barrier membranes in periodontal regeneration—"are the third generation membranes really here?". *JOURNAL OF CLINICAL AND DIAGNOSTIC RESEARCH*.
- Sancho-Vaello, E., Gil-Carton, D., François, P., Bonetti, E.-J., Kreir, M., Pothula, K. R., Kleinekathöfer, U., and Zeth, K. (2020). The structure of the antimicrobial human cathelicidin LL-37 shows oligomerization and channel formation in the presence of membrane mimics. *Scientific Reports*, 10(1).
- Schrödinger, LLC (2015). *The PyMOL Molecular Graphics System, Version 1.8*.
- Strutz, T. (2016). *Data Fitting and Uncertainty (2nd edition)*. Vieweg+Teubner.

- Tan, Z., Khakbaz, P., Chen, Y., Lombardo, J., Yoon, J. M., Shanks, J. V., Klauda, J. B., and Jarboe, L. R. (2017). Engineering escherichia coli membrane phospholipid head distribution improves tolerance and production of biorenewables. *Metabolic Engineering*, 44:1–12.
- Tao, W., Zhu, X., Yu, X., Zeng, X., Xiao, Q., Zhang, X., Ji, X., Wang, X., Shi, J., Zhang, H., and Mei, L. (2016). Black phosphorus nanosheets as a robust delivery platform for cancer theranostics. *Advanced Materials*, 29(1):1603276.
- Tokajuk, J., Deptuła, P., Piktel, E., Daniluk, T., Chmielewska, S., Wollny, T., Wolak, P., Fiedoruk, K., and Bucki, R. (2022). Cathelicidin LL-37 in health and diseases of the oral cavity. *Biomedicines*, 10(5):1086.
- Venable, R. M., Krämer, A., and Pastor, R. W. (2019). Molecular dynamics simulations of membrane permeability. *Chemical Reviews*, 119(9):5954–5997.
- Venable, R. M., Sodt, A. J., Rogaski, B., Rui, H., Hatcher, E., MacKerell, A. D., Pastor, R. W., and Klauda, J. B. (2014). CHARMM all-atom additive force field for sphingomyelin: Elucidation of hydrogen bonding and of positive curvature. *Biophysical Journal*, 107(1):134–145.
- Vishweshwaraiah, Y. L., Acharya, A., Hegde, V., and Prakash, B. (2021). Rational design of hyperstable antibacterial peptides for food preservation. *npj Science of Food*, 5(1).
- Xie, Z., Peng, M., Lu, R., Meng, X., Liang, W., Li, Z., Qiu, M., Zhang, B., Nie, G., Xie, N., Zhang, H., and Prasad, P. N. (2020). Black phosphorus-based photothermal therapy with aCD47-mediated immune checkpoint blockade for enhanced cancer immunotherapy. *Light: Science & Applications*, 9(1).
- Zhao, L., Cao, Z., Bian, Y., Hu, G., Wang, J., and Zhou, Y. (2018). Molecular dynamics simulations of human antimicrobial peptide LL-37 in model POPC and POPG lipid bilayers. *International Journal of Molecular Sciences*, 19(4):1186.

Appendices

A. Methodology

A.1 Parameter files (.mdp)

step6.0_minimization.mdp

```
1 define                = -DPOSRES -DPOSRES_FC_BB=4000.0 -DPOSRES_FC_SC=2000.0
  ↳ -DPOSRES_FC_LIPID=1000.0 -DDIHRES -DDIHRES_FC=1000.0
2 integrator            = steep
3 emtol                  = 1000.0
4 nsteps                 = 5000
5 nstlist                = 10
6 cutoff-scheme         = Verlet
7 rlist                  = 1.2
8 vdwtype                = Cut-off
9 vdw-modifier           = Force-switch
10 rvdw_switch           = 1.0
11 rvdw                   = 1.2
12 coulombtype           = PME
13 rcoulomb               = 1.2
14 ;
15 constraints            = h-bonds
16 constraint_algorithm   = LINCS
```

step6.1_equilibration.mdp

```
1 define                = -DPOSRES -DPOSRES_FC_BB=4000.0 -DPOSRES_FC_SC=2000.0
  ↪ -DPOSRES_FC_LIPID=1000.0 -DDIHRES -DDIHRES_FC=1000.0
2 integrator           = md
3 dt                   = 0.001
4 nsteps               = 125000
5 nstxtcout            = 5000
6 nstvout              = 5000
7 nstfout              = 5000
8 nstcalcenergy        = 100
9 nstenergy             = 1000
10 nstlog               = 1000
11 ;
12 cutoff-scheme        = Verlet
13 nstlist              = 20
14 rlist                = 1.2
15 vdwttype             = Cut-off
16 vdw-modifier         = Force-switch
17 rvdw_switch          = 1.0
18 rvdw                 = 1.2
19 coulombtype          = PME
20 rcoulomb             = 1.2
21 ;
22 tcoupl               = v-rescale
23 tc_grps              = SOLU MEMB SOLV
24 tau_t                = 1.0 1.0 1.0
25 ref_t                = 310.15 310.15 310.15
26 ;
27 constraints           = h-bonds
28 constraint_algorithm = LINCS
29 ;
30 nstcomm              = 100
31 comm_mode            = linear
32 comm_grps            = SOLU_MEMB SOLV
33 ;
34 gen-vel              = yes
35 gen-temp              = 310.15
36 gen-seed              = -1
```

step6.2_equilibration.mdp

```
1 define                = -DPOSRES -DPOSRES_FC_BB=2000.0 -DPOSRES_FC_SC=1000.0
  → -DPOSRES_FC_LIPID=400.0 -DDIHRES -DDIHRES_FC=400.0
2 integrator           = md
3 dt                   = 0.001
4 nsteps               = 125000
5 nstxtcout            = 5000
6 nstvout              = 5000
7 nstfout              = 5000
8 nstcalcenergy        = 100
9 nstenergy            = 1000
10 nstlog               = 1000
11 ;
12 cutoff-scheme        = Verlet
13 nstlist              = 20
14 rlist                = 1.2
15 vdwttype             = Cut-off
16 vdw-modifier         = Force-switch
17 rvdw_switch          = 1.0
18 rvdw                 = 1.2
19 coulombtype          = PME
20 rcoulomb             = 1.2
21 ;
22 tcoupl               = v-rescale
23 tc_grps              = SOLU MEMB SOLV
24 tau_t                = 1.0 1.0 1.0
25 ref_t                = 310.15 310.15 310.15
26 ;
27 constraints          = h-bonds
28 constraint_algorithm = LINCS
29 continuation        = yes
30 ;
31 nstcomm              = 100
32 comm_mode            = linear
33 comm_grps            = SOLU_MEMB SOLV
```

step6.3_equilibration.mdp

```
1  define                = -DPOSRES -DPOSRES_FC_BB=1000.0 -DPOSRES_FC_SC=500.0
   ↪ -DPOSRES_FC_LIPID=400.0 -DDIHRES -DDIHRES_FC=200.0
2  integrator            = md
3  dt                    = 0.001
4  nsteps                = 125000
5  nstxtcout             = 5000
6  nstvout               = 5000
7  nstfout               = 5000
8  nstcalcenergy         = 100
9  nstenergy             = 1000
10 nstlog                = 1000
11 ;
12 cutoff-scheme         = Verlet
13 nstlist                = 20
14 rlist                  = 1.2
15 vdwtpe                 = Cut-off
16 vdw-modifier           = Force-switch
17 rvdw_switch            = 1.0
18 rvdw                   = 1.2
19 coulombtype            = PME
20 rcoulomb               = 1.2
21 ;
22 tcoupl                 = v-rescale
23 tc_grps                 = SOLU MEMB SOLV
24 tau_t                  = 1.0 1.0 1.0
25 ref_t                   = 310.15 310.15 310.15
26 ;
27 pcoupl                 = c-rescale
28 pcoupltype             = semiisotropic
29 tau_p                   = 5.0
30 compressibility         = 4.5e-5 4.5e-5
31 ref_p                   = 1.0 1.0
32 refcoord_scaling       = com
33 ;
34 constraints            = h-bonds
35 constraint_algorithm    = LINCS
36 continuation           = yes
37 ;
38 nstcomm                 = 100
39 comm_mode               = linear
40 comm_grps              = SOLU_MEMB SOLV
```


step6.4_equilibration.mdp

```
1 define                = -DPOSRES -DPOSRES_FC_BB=500.0 -DPOSRES_FC_SC=200.0
  → -DPOSRES_FC_LIPID=200.0 -DDIHRES -DDIHRES_FC=200.0
2 integrator           = md
3 dt                   = 0.002
4 nsteps               = 250000
5 nstxtcout            = 5000
6 nstvout              = 5000
7 nstfout              = 5000
8 nstcalcenergy        = 100
9 nstenergy            = 1000
10 nstlog               = 1000
11 ;
12 cutoff-scheme       = Verlet
13 nstlist              = 20
14 rlist               = 1.2
15 vdwtype              = Cut-off
16 vdw-modifier         = Force-switch
17 rvdw_switch         = 1.0
18 rvdw                 = 1.2
19 coulombtype          = PME
20 rcoulomb             = 1.2
21 ;
22 tcoupl               = v-rescale
23 tc_grps              = SOLU MEMB SOLV
24 tau_t                = 1.0 1.0 1.0
25 ref_t                = 310.15 310.15 310.15
26 ;
27 pcoupl               = c-rescale
28 pcoupltype           = semiisotropic
29 tau_p                = 5.0
30 compressibility       = 4.5e-5 4.5e-5
31 ref_p                 = 1.0 1.0
32 refcoord_scaling     = com
33 ;
34 constraints           = h-bonds
35 constraint_algorithm = LINCS
36 continuation         = yes
37 ;
38 nstcomm               = 100
39 comm_mode             = linear
40 comm_grps             = SOLU_MEMB SOLV
```

step6.5_equilibration.mdp

```
1 define                = -DPOSRES -DPOSRES_FC_BB=200.0 -DPOSRES_FC_SC=50.0
  ↪ -DPOSRES_FC_LIPID=40.0 -DDIHRES -DDIHRES_FC=100.0
2 integrator           = md
3 dt                   = 0.002
4 nsteps               = 250000
5 nstxtcout            = 5000
6 nstvout              = 5000
7 nstfout              = 5000
8 nstcalcenergy        = 100
9 nstenergy             = 1000
10 nstlog               = 1000
11 ;
12 cutoff-scheme        = Verlet
13 nstlist              = 20
14 rlist                = 1.2
15 vdwtype              = Cut-off
16 vdw-modifier          = Force-switch
17 rvdw_switch          = 1.0
18 rvdw                 = 1.2
19 coulombtype           = PME
20 rcoulomb              = 1.2
21 ;
22 tcoupl               = v-rescale
23 tc_grps              = SOLU MEMB SOLV
24 tau_t                = 1.0 1.0 1.0
25 ref_t                = 310.15 310.15 310.15
26 ;
27 pcoupl               = c-rescale
28 pcoupltype           = semiisotropic
29 tau_p                = 5.0
30 compressibility       = 4.5e-5 4.5e-5
31 ref_p                = 1.0 1.0
32 refcoord_scaling     = com
33 ;
34 constraints           = h-bonds
35 constraint_algorithm = LINCS
36 continuation         = yes
37 ;
38 nstcomm              = 100
39 comm_mode             = linear
40 comm_grps            = SOLU_MEMB SOLV
```

step6.6_equilibration.mdp

```
1 define                = -DPOSRES -DPOSRES_FC_BB=50.0 -DPOSRES_FC_SC=0.0
  → -DPOSRES_FC_LIPID=0.0 -DDIHRES -DDIHRES_FC=0.0
2 integrator           = md
3 dt                   = 0.002
4 nsteps               = 250000
5 nstxtcout            = 5000
6 nstvout              = 5000
7 nstfout              = 5000
8 nstcalcenergy        = 100
9 nstenergy            = 1000
10 nstlog               = 1000
11 ;
12 cutoff-scheme        = Verlet
13 nstlist              = 20
14 rlist                = 1.2
15 vdwtpe               = Cut-off
16 vdw-modifier         = Force-switch
17 rvdw_switch          = 1.0
18 rvdw                 = 1.2
19 coulombtype          = PME
20 rcoulomb             = 1.2
21 ;
22 tcoupl               = v-rescale
23 tc_grps              = SOLU MEMB SOLV
24 tau_t                = 1.0 1.0 1.0
25 ref_t                = 310.15 310.15 310.15
26 ;
27 pcoupl               = c-rescale
28 pcoupltype           = semiisotropic
29 tau_p                = 5.0
30 compressibility      = 4.5e-5 4.5e-5
31 ref_p                = 1.0 1.0
32 refcoord_scaling     = com
33 ;
34 constraints          = h-bonds
35 constraint_algorithm = LINCS
36 continuation        = yes
37 ;
38 nstcomm              = 100
39 comm_mode            = linear
40 comm_grps            = SOLU_MEMB SOLV
```

step7_equilibration.mdp

```
1  integrator          = md
2  dt                  = 0.002
3  nsteps              = 500000000
4  nstxout             = 50000
5  nstvout             = 50000
6  nstfout             = 50000
7  nstcalcenergy      = 100
8  nstenergy           = 1000
9  nstlog              = 1000
10 ;
11 cutoff-scheme       = Verlet
12 nstlist              = 20
13 rlist                = 1.2
14 vdwtype              = Cut-off
15 vdw-modifier         = Force-switch
16 rvdw_switch         = 1.0
17 rvdw                 = 1.2
18 coulombtype         = PME
19 rcoulomb             = 1.2
20 ;
21 tcoupl               = Nose-Hoover
22 tc_grps              = SOLU MEMB SOLV
23 tau_t                = 1.0 1.0 1.0
24 ref_t                = 310.15 310.15 310.15
25 ;
26 pcoupl               = Parrinello-Rahman
27 pcoupltype           = semiisotropic
28 tau_p                = 5.0
29 compressibility      = 4.5e-5 4.5e-5
30 ref_p                = 1.0 1.0
31 ;
32 constraints          = h-bonds
33 constraint_algorithm = LINCS
34 continuation        = yes
35 ;
36 nstcomm              = 100
37 comm_mode            = linear
38 comm_grps            = SOLU_MEMB SOLV
```

B. Results and Discussion

B.1 Lipid tail order PCA analysis

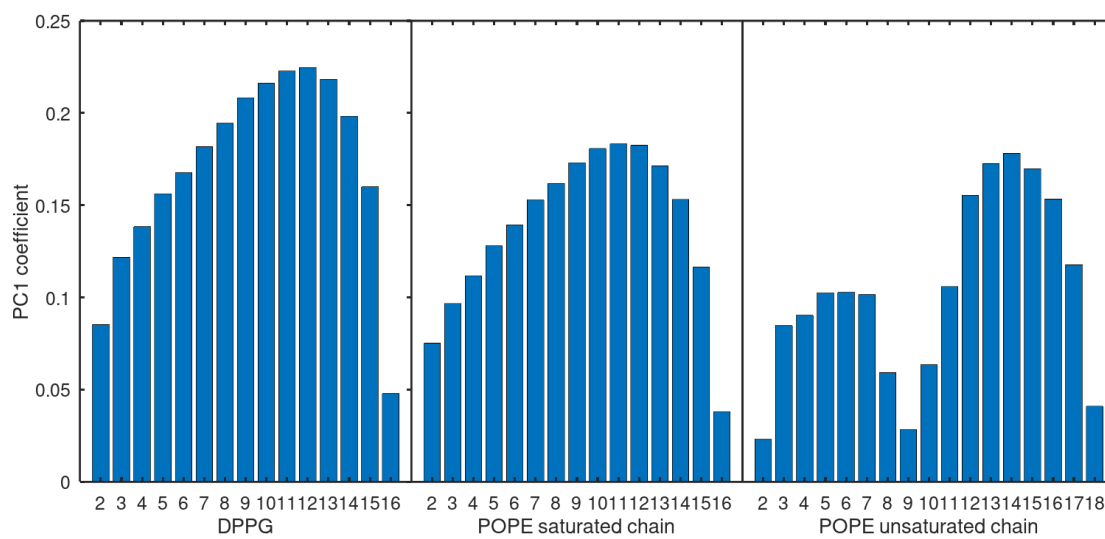


Figure B.1: PC1 coefficients for the S_{CH} PCA analysis.

B.2 Permeability – Poisson point process

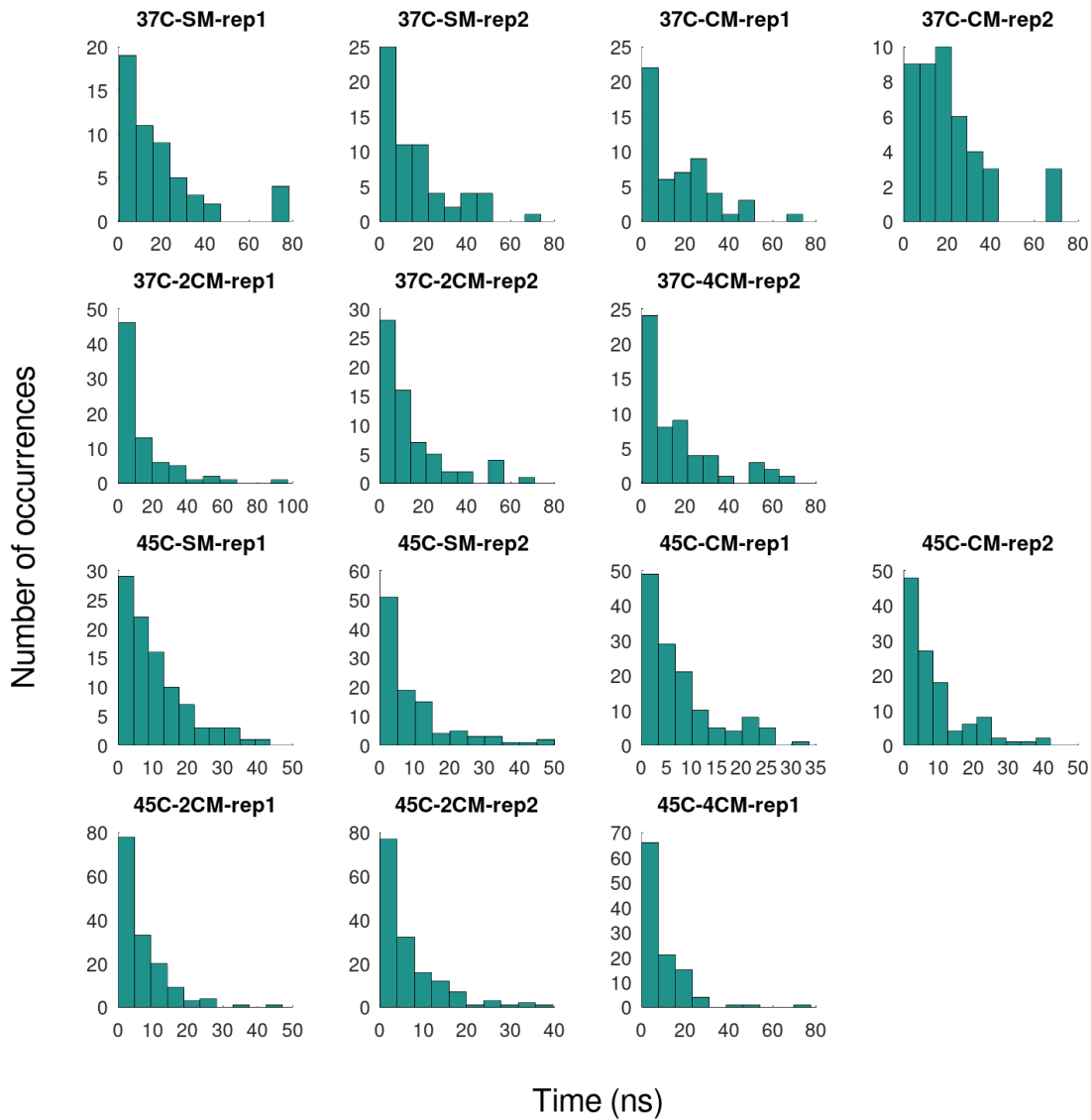


Figure B.2: Histograms of inter-event times distributions.

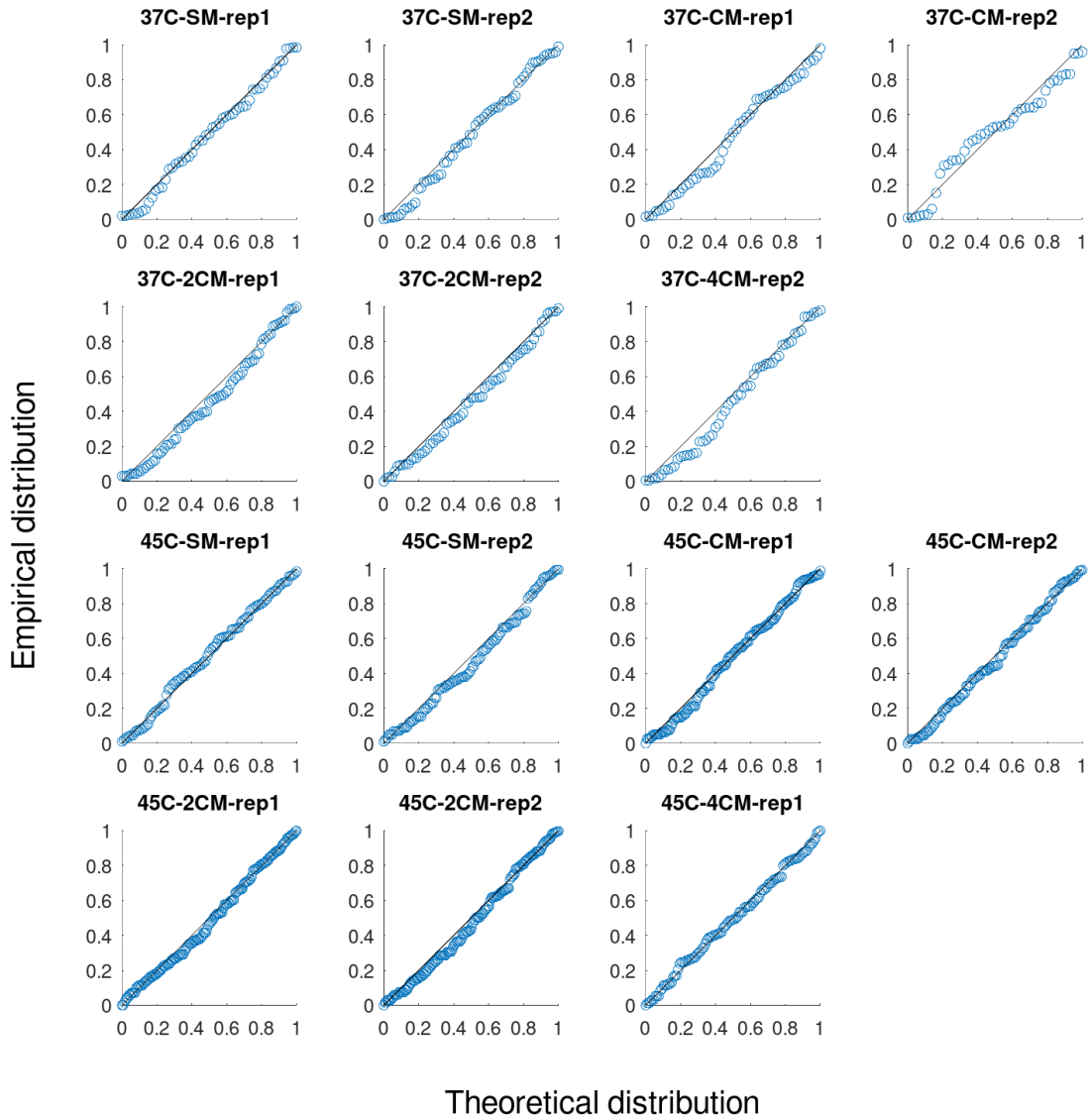


Figure B.3: P-P plot for the fitting of inter-event times to an exponential distribution.